AGU PUBLICATIONS

JGR

Journal of Geophysical Research: Solid Earth

RESEARCH ARTICLE

10.1002/2014JB011217

Key Points:
- Noise is trapped in a cavity-like structure associated with a fault zone
- Trapped noise emerges under broader conditions than trapped ballistic waves
- A near-field focal spot is reconstructed from the isotropic in-fault wavefield

Supporting Information:
- Readme
- Figures S1–S7

Correspondence to:
G. Hillers,
gregor.hillers@ujf-grenoble.fr

Citation:
Hillers, G., M. Campillo, Y. Ben-Zion, and P. Roux (2014), Seismic fault zone trapped noise, *J. Geophys. Res. Solid Earth*, *119*, doi:10.1002/2014JB011217.

Received 21 APR 2014
Accepted 19 JUN 2014
Accepted article online 25 JUN 2014

Seismic fault zone trapped noise

G. Hillers[1], M. Campillo[1], Y. Ben-Zion[2], and P. Roux[1]

[1]Institut des Sciences de la Terre, Université Joseph Fourier, Grenoble, France, [2]Department of Earth Sciences, University of Southern California, Los Angeles, California, USA

Abstract Systematic velocity contrasts across and within fault zones can lead to head and trapped waves that provide direct information on structural units that are important for many aspects of earthquake and fault mechanics. Here we construct trapped waves from the scattered seismic wavefield recorded by a fault zone array. The frequency-dependent interaction between the ambient wavefield and the fault zone environment is studied using properties of the noise correlation field. A critical frequency $f_c \approx 0.5$ Hz defines a threshold above which the in-fault scattered wavefield has increased isotropy and coherency compared to the ambient noise. The increased randomization of in-fault propagation directions produces a wavefield that is trapped in a waveguide/cavity-like structure associated with the low-velocity damage zone. Dense spatial sampling allows the resolution of a near-field focal spot, which emerges from the superposition of a collapsing, time reversed wavefront. The shape of the focal spot depends on local medium properties, and a focal spot-based fault normal distribution of wave speeds indicates a ~50% velocity reduction consistent with estimates from a far-field travel time inversion. The arrival time pattern of a synthetic correlation field can be tuned to match properties of an observed pattern, providing a noise-based imaging tool that can complement analyses of trapped ballistic waves. The results can have wide applicability for investigating the internal properties of fault damage zones, because mechanisms controlling the emergence of trapped noise have less limitations compared to trapped ballistic waves.

1. Introduction

The ambient seismic noise field has been used extensively in the last decade to image numerous structures across a wide range of spatial scales covering the crust, lithosphere, upper mantle, and the Earth core [*Vandemeulebrouck et al.*, 2009; *Shapiro et al.*, 2005; *Stehly et al.*, 2009; *Verbeke et al.*, 2012; *Boué et al.*, 2013; *Lin et al.*, 2013]. Noise-based imaging requires that the ambient wavefield is sufficiently isotropic [*Weaver et al.*, 2009]. In seismology, source averaging replaces the theoretical ensemble average over the disorder, i.e., wavefield isotropy is predominantly controlled by the excitation patterns. The applicability of noise-based imaging further benefits from randomization of propagation directions through scattering and mode conversions. Seismic heterogeneities control the efficiency of wave diffusion in environments ranging from relatively homogeneous cratonic areas [*Poli et al.*, 2013] to highly scattering volcanic edifices [*Wegler*, 2003] and fault zone (FZ) regions [*Hong and Menke*, 2006; *Hillers et al.*, 2013].

The ambient seismic wavefield in a FZ environment is characterized by frequency-dependent superposition of scattered, guided, bended, and reflected surface and body wave components. Several studies used correlations of ambient seismic noise to image FZ environments [*Roux et al.*, 2005; *Roux*, 2009; *Hillers et al.*, 2013; *Zigone et al.*, 2014] at wavelengths (λ) that are large compared to the width of the low-velocity FZ damage zone (λ_0). Fault zone head and trapped waves propagating along velocity contrast interfaces and the damage zone provide high-resolution information on the internal components of fault structures [*Ben-Zion and Aki*, 1990; *Li et al.*, 1990; *Lewis and Ben-Zion*, 2010]. Here we extract signatures associated with fault zone trapped noise from the ambient seismic field using data recorded across the Calico fault zone in California. The results provide an important new high-resolution tool for imaging the internal structure of fault damage zones. Significantly different wavefield properties within and outside the FZ reflect the trapped nature of the wavefield at frequencies above a critical value for noise-FZ interaction (f_c). Properties of noise correlation functions can be understood in the context of time-reversal experiments [*Cassereau and Fink*, 1992; *Derode et al.*, 2001] and suggest that the low-velocity zone (LVZ) acts as a waveguide [*Ben-Zion and Aki*, 1990; *Roux et al.*, 2008] or a reverberant cavity [*Lobkis and Weaver*, 2001; *Catheline et al.*, 2008]. The noise-based method developed and applied here can have wider applicability than methods based on ballistic fault zone

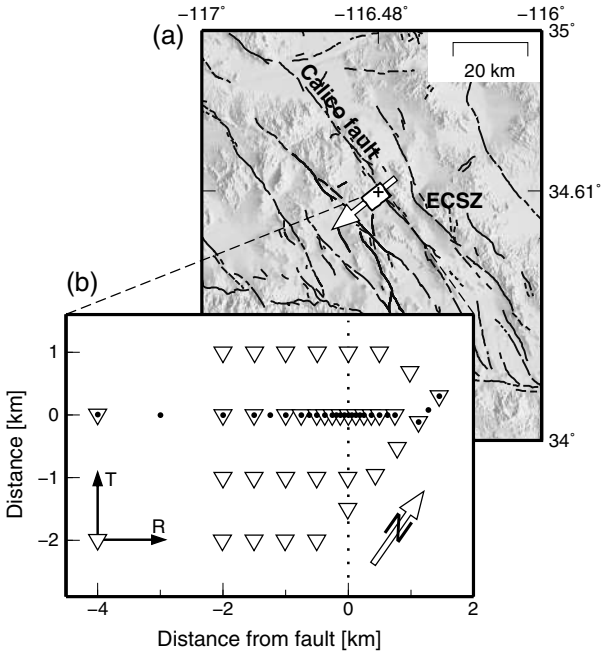

Figure 1. (a) Shaded relief map of the Eastern California Shear Zone (ECSZ) surrounding the Calico fault zone array. The arrow is oriented normal to the fault and points toward the Pacific coastline, which is the direction from which noise impinges on the fault. The arrow is aligned with the horizontal dotted lines in Figures 4b and 4c. Black lines show geologically mapped faults. (b) Rotated array geometry. The array position is indicated in Figure 1a by the white box, where the cross sign marks the origin. Triangles and dots denote broadband and short period sensors, respectively. The fault trace (dotted line) is estimated from maximum interferometric synthetic aperture radar strain [*Fialko*, 2004] and deviates from mapped surface fault strands. R and T indicate fault radial and transverse directions. The variable x used in section 4 is associated with the abscissa.

waves since it does not depend on the limited existence of appropriate ballistic sources [*Jahnke et al.*, 2002; *Fohrmann et al.*, 2004; *Lewis and Ben-Zion*, 2010].

2. Location, Data, and Methods

We analyze frequency-dependent noise-FZ interactions by processing data of a dense seismic array installed across the Calico fault [*Cochran et al.*, 2009], one of several ∼35°NW oriented, subparallel strike-slip faults in the Eastern California Shear Zone (Figure 1a). The wide ($\lambda_0 \approx$ 1–2 km) compliant fault damage zone around the mapped surface trace is characterized by a shear modulus reduction of factor 2 compared to the more competent host rock [*Fialko*, 2004]. Fault zone trapped waves excited by local earthquakes and shots [*Cochran et al.*, 2009] indicate that the structure of the low-velocity waveguide is sufficiently continuous in the along-strike direction [*Igel et al.*, 1997] on length scales associated with the hypocenter distances (O(10 km)). The strong velocity contrast across the LVZ boundaries further leads to multiple fault-internal body wave reflections [*Yang et al.*, 2011]. Together, these ballistic phases indicate that the LVZ is characterized by a north dipping P wave velocity contrast of 40–60% down to 5 km depth. In addition to the analyses of these phases, continuous data recorded by the network have been processed to study short-period noise excitation along the Pacific coastline [*Zhang et al.*, 2009] and local-scale noise propagation properties [*Zhang and Gerstoft*, 2014].

The data were acquired by a temporary field experiment consisting of a 2-D broadband array and a collocated short-period line, which cover the damage zone and an area ∼2 km SW to the fault (Figure 1b). The minimum interstation distance of broadband and short-period sensors normal to the fault strike is 50 m and 25 m, respectively. The horizontal components are oriented normal to the fault strike (Figure 1b), with channel denoted R pointing at 55° (radial), and channel T pointing at 325° (transversal). The letters T′ and R′ denote these components after application of the Optimal Rotation Algorithm (section 2.5). The network recorded between Julian days (JD) ∼150 and ∼330 in 2006. We retrieve the complete data set from the Incorporated Research Institutions for Seismology (IRIS) facility [*Scheingraber et al.*, 2013], but we focus on ∼90 days beginning JD 235 when both the complete 2-D array and the line were continuously recording.

We apply multiple processing and analysis techniques to decipher the complex, frequency-dependent wave propagation situation in a challenging FZ environment. In the remainder of this section, we discuss general and technical aspects associated with estimates of kinetic noise energy ratios, details of the correlation procedure, spectral properties of noise correlations, correlation-based beamforming, and the Optimal Rotation Algorithm (ORA). Readers familiar with these applications can continue to section 3. Based on the results obtained with the multicomponent analysis, we estimate the fault-normal velocity structure in section 4. Construction of synthetic correlation fields for FZ imaging is detailed in section 5.

2.1. Kinetic Energy Ratio

A stable ratio of shear and longitudinal deformation energy indicates that mode conversion through scattering is balanced [*Weaver*, 1982; *Shapiro et al.*, 2000; *Hennino et al.*, 2001; *Margerin et al.*, 2009; *Sánchez-Sesma et al.*, 2011] and that energy propagation can be described by a diffusion process. The ratio itself is a consequence of scattering and absorption properties. The kinetic energy ratio H^2/V^2 can be used as an alternative proxy [*Hennino et al.*, 2001; *Sánchez-Sesma et al.*, 2011] and is generally easier to compute than estimates of the deformation energy [*Shapiro et al.*, 2000]. H^2 and V^2 denote squared velocity amplitudes recorded on the horizontal components and the vertical component, respectively. To avoid analysis of the entire data set, we estimate H^2/V^2 ratios using continuous short-period data from 20 randomly chosen days. At each of these days we randomly choose 3 h of band-pass filtered data from which we compute $H^2 = h_1^2 + h_2^2$ and $V^2 = Z^2$, where $h_{1,2}$ and Z denote data from the two horizontal channels and the vertical channel. The traces are smoothed with a moving average of length Δt s separated by dt s, the inverse of the upper limit of the frequency band. Ideally, Δt is of the order of the mean free time [*Shapiro et al.*, 2000; *Hennino et al.*, 2001], which is, however, difficult to estimate [*Campillo*, 2006]. We test a wide range of constant and frequency-dependent Δt values and compare estimates associated with multiple selections of the randomly drawn time windows. We find insensitivity to choices associated with smoothing and timing parameters. This indicates that the obtained H^2/V^2 statistics are related to local material properties and are not biased by transient changes of wavefield properties.

2.2. Noise Correlations

With the exception of the H^2/V^2 ratios, our conclusions are based on analysis of noise correlation functions. Correlation moveout patterns contain information on propagation directions and speeds, and particle motions indicate wave polarization and can help to constrain wavefield constituents.

Here we compute only intraarray correlations, i.e., we correlate only between the broadband or the short-period sensors, but considering potential interarray applications, we first removed the instrument response and homogenized the sampling rate to 50 Hz. Further, data processing steps generally target the optimization of the correlation signal-to-noise (SNR) ratio by minimizing bias associated with nonstationary components of the wavefield. Our strategy includes spectral whitening and amplitude clipping at 3 times the standard deviation of the amplitude distribution in a multihour yet subdaily time window, and we remove windows containing suspiciously large amplitudes indicative of earthquakes [*Poli et al.*, 2012a, 2012b; *Boué et al.*, 2013; *Hillers et al.*, 2014]. The application of whitening and amplitude clipping reduces biasing effects of variable noise spectral power and potential band-limited transients. We tested other strategies neglecting spectral normalization but including 1 bit temporal normalization and found that the choices emphasize different constituents of the wavefield and can have significant effects on the resulting correlation patterns and responses of the associated correlation-based beamforming (section 2.4). However, here we are concerned with estimates of the coherency and thus focus on whitened and clipped seismograms. We compute daily coherency estimates between two stations A and B, $C_{AB}(\tau)$, i.e., the time domain equivalence of

$$\gamma_{AB}(\omega) = \left\langle \frac{u_A(\omega) u_B^*(\omega)}{\{|u_A(\omega)|\}\{|u_B(\omega)|\}} \right\rangle . \quad (1)$$

Here τ denotes lapse time, ω angular frequency, $u_{A,B}$ seismograms at stations A and B, and the asterisk represents complex conjugate. Curly brackets $\{\cdot\}$ indicate a spectral average, i.e., the cross spectrum is scaled by the total energy of the signals recorded at A and B. The brackets $\langle\cdot\rangle$ mean either an ensemble average over the disorder or a time/frequency average of a single realization or averaging of fields produced by a set of sources [*Campillo*, 2006]. The latter situation applies in seismology, where source-averaging is realized by temporal averaging. That is, the (unscaled) correlation in the time domain can be expressed as $C_{AB}(\tau) = \langle u_A(t), u_B(t) \rangle_T$, where $\langle\cdot\rangle_T$ denotes correlation over the time interval T, and $T \to \infty$. All daily correlations are stacked over the $T = 90$ day observation period.

Preprocessing includes whitening in a wide frequency range (0.05–10 Hz) for the broadband records. Frequency-dependent analyses performed on these data (beamforming and ORA) are achieved by applying a band-pass filter to the broadband correlations. Note that beamforming and the ORA are only weakly sensitive to the precise value of the correlation amplitudes. In contrast, the focal width method (sections 3.3 and 4.1) applied to the short-period data for local estimates of the wave speed and length requires unbiased

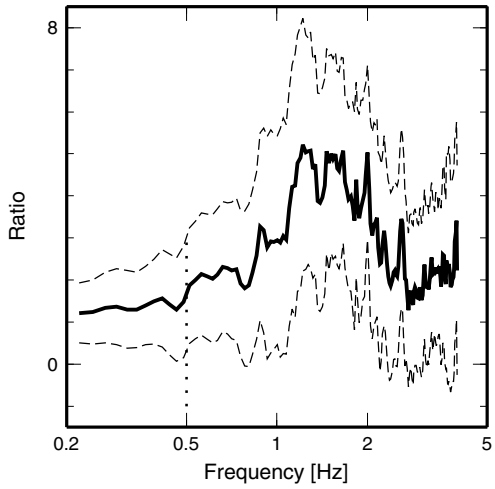

Figure 2. Average amplitude spectra of windowed ([−20, 20] s) in-fault ZZ correlation functions scaled by an average constructed from correlation pairs located outside the fault zone. One standard deviation is indicated by the dashed lines. The distribution indicates a sensitivity of the noise wavefield to the structure of the low-velocity zone above the critical frequency for interaction, $f_c \approx 0.5$ Hz. The scale on the abscissa is logarithmic.

estimates of amplitude. To avoid biases associated with the spectral properties of the constructed coherency estimates, short-period data are narrow-band whitened prior to correlation.

It should be noted that ZZ and TT correlations both represent motion that is excited and recorded orthogonal to the fault-normal direction. We find that ZZ and TT patterns are often very similar and that TT correlations are frequently characterized by better SNR compared to the ZZ functions. Moreover, particle motion in the TR-TT plane is often equivalent to trajectories in the more familiar ZR-ZZ plane, which permits the distinction of body and surface waves based on ellipticity [*Landès et al.*, 2010].

2.3. Critical Frequency for Interaction

Coherency power spectra indicate the frequency-dependent distribution of coherent energy built up by correlation. Generally, peak values correspond to double-frequency microseism excitation around 0.2 Hz, beyond which the spectrum falls off toward higher frequencies. To assess the spectral shape in the Calico FZ environment, we analyze correlations from all broadband station pairs. From systematic differences between spectra associated with station pairs inside and outside the LVZ, a critical frequency for interaction can be estimated above which the wavefield is affected by the low-velocity structure. The location and extension of the LVZ is estimated from previous analyses [*Cochran et al.*, 2009], which is compatible with our noise-based results discussed below. The results (Figure 2) show that the wavefields differ significantly across ~0.5 Hz, indicating that there is increased coherent energy within the LVZ. Particular wavefield properties in the 1–2 Hz range are implied by the peak of the distribution, and the distinctiveness of this frequency band is confirmed by several observations in our analysis. It should be noted that the station density does not bias this conclusion due to potentially increased attenuation associated with larger distances outside the fault or the sampling of the large-amplitude focal spot within the fault. Spectral properties of trapped waves exhibit the same sensitivity to the FZ structure (Figure S1 in the supporting information), which is a strong indicator of a consistent critical frequency for interaction $f_c \approx 0.5$ Hz that applies to ballistic and scattered wavefields alike. With an appropriate velocity model, the effective width of the velocity reduction of the LVZ can be estimated from f_c. We consider this threshold in the following frequency-dependent analysis.

2.4. Beamforming

We apply conventional plane wave beamforming to ZZ correlation functions. Beamforming on seismic noise records usually consists of processing up to several hours long seismograms to accumulate a coherent phase signal in the cross spectral density matrix [*Gerstoft and Tanimoto*, 2007; *Roux*, 2009; *Hillers et al.*, 2012]. Accumulation of coherent energy is similarly achieved by the correlation procedure. The correlation-based beamforming performed here constitutes a spectral delay-and-sum approach applied to time series—correlation functions—that are short compared to the original noise seismograms. The method resolves the strongest, i.e., most coherent arrival, in contrast to statistical estimates [*Wagner*, 1998] that can isolate multiple superimposed components of variable strength and directivity [*Vandemeulebrouck et al.*, 2009]. As demonstrated below, the Calico FZ wavefield constitutes such a complex situation. It should therefore be noted that correlation-beamforming in the present context is sensitive to normalization strategies (section 2.2) and that beams formed from seismograms or correlations can differ because of data processing choices.

In standard array beamforming techniques, the network center is usually chosen as the reference point. Here we assign the reference station S_{ref} (station A in equation (1)) of each correlation pair as the origin for the phase delay estimate, which emphasizes the assumption of a model plane wave propagating with constant

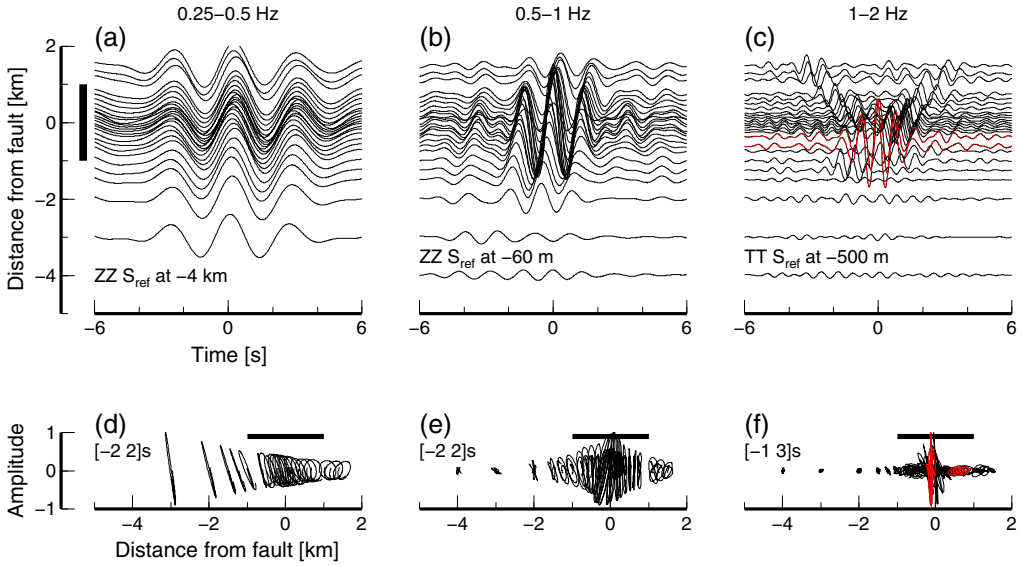

Figure 3. (a–c) Frequency-dependent correlation amplitude and (d–f) polarization patterns constructed from fault-normal short-period data (ordinate in a–c corresponds to abscissa in Figure 1b). Energy at negative (positive) times propagates toward (away from) the correlation reference station S_{ref}. Moveout patterns illustrate variable noise-FZ interactions, ranging from a transparent fault at low frequencies (a) to the symmetric in-fault signature of trapped noise (c). Traces are scaled to their maximum in Figure 3a or to the pattern maximum in Figures 3b and 3c; large amplitudes associated with the focal spot are highlighted in Figure 3c. See Figure S5 for complementary patterns. All polarization patterns in Figures 3d–3f show radial-vertical ZR-ZZ motion in the fault-normal direction (abscissa corresponds to abscissa in Figure 1b). Values are scaled to the pattern maximum, and radial and vertical amplitude scales are equal. The position of S_{ref} and the indicated time windows correspond to the moveout patterns above. In Figure 3f the polarization of the focal spot and the surface wave are highlighted.

velocity across the network. Considering frequency-dependent wavefield properties within and outside the FZ, we use frequency-dependent subarrays consisting of all stations at low frequencies, and in-fault stations for $f > f_c$ (Figure S2). To avoid bias associated with the dense spatial sampling of the centerline (Figure 1b), we homogenize the spatial sampling in all directions.

2.5. The Optimal Rotation Algorithm

The Optimal Rotation Algorithm (ORA) [*Roux*, 2009] minimizes energy on the transverse components ZT, TZ, RT, and TR of the correlation tensor by allowing each station to freely realign in the incident noise direction (Figure S3). It assumes that Love and Rayleigh waves impinge on a network with the same propagation direction, and the alignment is intended to make the noise-correlation tensor compatible with a surface wave Green's tensor. The minimization of energy is achieved by virtually rotating the coordinate system at stations A and B around two independent azimuths Ψ_A and Ψ_B and around two corresponding tilt angles. Tensor-optimizing tilt angles are usually small and can be neglected, so that Ψ distributions provide the dominant information about pair-dependent surface wave propagation directions. Application of the ORA to the dense broadband station line (16 stations) yields 120 Ψ_A, Ψ_B, and residual estimates associated with the 120 possible pairs (Figure S4). The residuals measure the energy on transversal traces that could not be suppressed by the virtual rotation. From these data, we construct average long-range and short-range fault-normal profiles (supporting information) that synthesize the information on horizontal propagation directions.

3. Results

3.1. Low-Frequency Regime: Superposition of Wavefield Constituents

Low-frequency ($f < f_c$) fault-normal ZZ and TT correlation arrival patterns are characterized by a pulse with high apparent velocity, $v_a \approx$ 8–10 km/s (Figure 3a). When the reference correlation station S_{ref} is located within the LVZ, consistent longitudinal polarization in the radial-vertical (ZR-ZZ) plane indicates a *P* wave arrival. If S_{ref} is located on either side of the LVZ, we observe a gradual change of the longitudinal to an elliptical motion associated with Rayleigh surface wave propagation (Figure 3d).

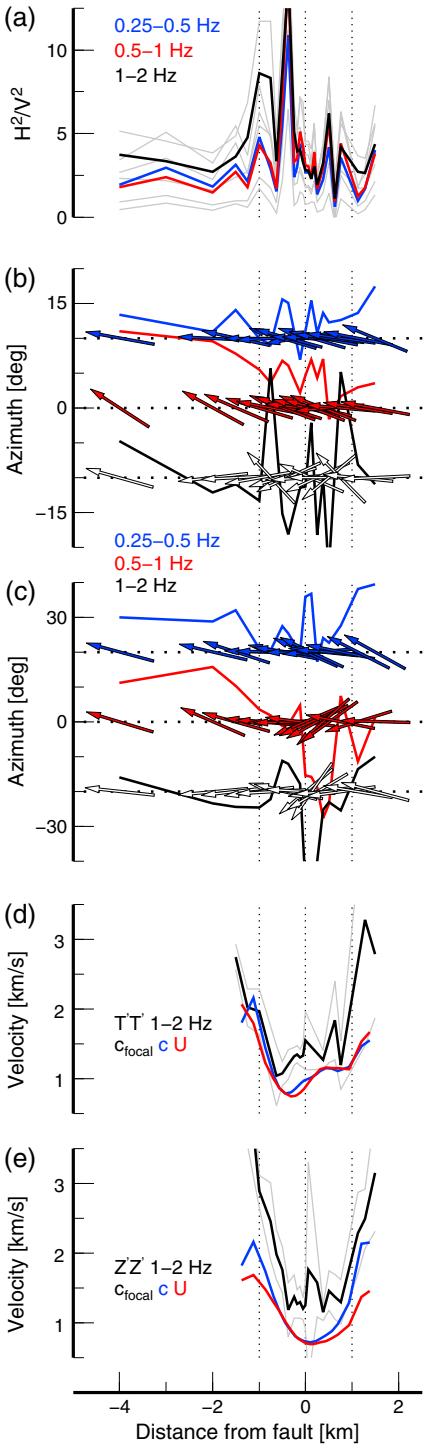

A similar spatial change of longitudinal motion to progressively more circular particle trajectories is also observed for other component combinations. The distribution of kinetic energy ratios (Figure 4a) supports the hypothesis that fault-normal wavefield variations control the observed complex mixture of body and surface wave components.

Beamforming and application of the ORA can constrain individual modes of the composite wavefield. Conventional beamforming assuming a plane wave is, however, challenged by the mixture of multiple propagation modes. The 2-D ZZ correlation field is dominated by surface wave energy propagating SE→NW along the fault strike at $v_a \approx 1$ km/s (Figure 5a). In contrast, beamforming on all ZZ correlations from the dense fault-normal line extracts arrivals associated with SW→NE *P* propagation with $v_a \approx 4$–5 km/s. The long-range ORA synthesis (Figure 4b, blue) also indicates energy arriving from westward azimuths approximately normal to the fault, which is compatible with excitation along the Pacific coastline [*Schulte-Pelkum et al.*, 2004; *Stehly et al.*, 2006; *Gerstoft and Tanimoto*, 2007; *Zhang et al.*, 2009; *Hillers et al.*, 2013]. The short-range average (Figure 4c, blue) shows that the incident propagation is relatively insensitive to the LVZ, which is also confirmed by the similarity of motion patterns in the station reference frame and the optimally rotated frame.

Combined, these results imply that the low-frequency ambient wavefield is characterized by a superposition of body and surface waves and a mixture of ambient propagation directions associated with oceanic excitation and components that move along the FZ strike. The SE→NW propagation indicates sensitivity to the structure at $f < f_c$, i.e., at $\lambda > \lambda_0$, which can partially be controlled by regional deformation-related anisotropy indicated by subparallel faults SW and NE to the Calico fault (Figure 1a).

Figure 4. Fault-normal distributions of wavefield and fault zone properties. The abscissa corresponds to abscissa in Figure 1b. (a) Variations of spectral ratios H^2/V^2 are strongest in the region of the SW velocity gradient. (b) Long-range and (c) short-range averages of propagation directions based on the Optimal Orientation Algorithm are indicated by graphs and arrows. The ordinate corresponds to the graphs which are offset by [10, 0, -10] (Figure 4b) and [-20, 0, 20] (Figure 4c); the zero levels are indicated by the dotted lines and correspond to the fault-normal direction indicated by the arrow in Figure 1a. Zero azimuth indicates propagation perpendicular to the fault. Orientation of arrows is exaggerated by a factor 3 in Figure 4b and 1.5 in Figure 4c for better visibility of the fault-normal trends. (d and e) Phase (*c*) and group (*U*) velocity profiles obtained from focal spot properties and an inversion of *c* and *U* arrival time estimates as in Figure 3c. T′T′ and Z′Z′ results in Figures 4d and 4e are based on the ORA-rotated correlation field.

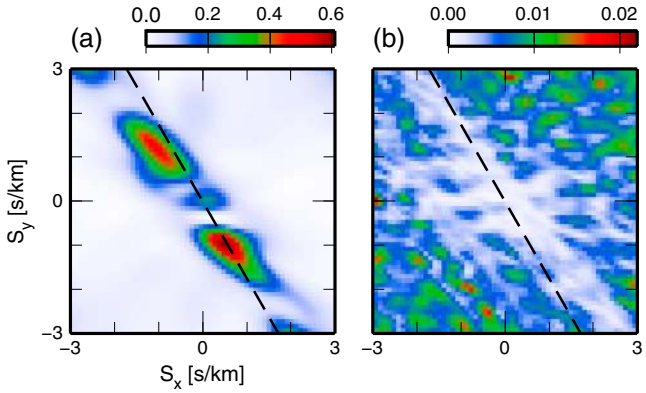

Figure 5. Horizontal slowness maps obtained with correlation-based beamforming from (a) 0.25–0.5 Hz to (b) 1–2 Hz ZZ correlations. The dashed line denotes the approximate orientation of the Calico fault strike. In Figure 5a energy travels in SE→NW directions. Energy in the opposite NW quadrant is an aliasing artifact (Figure S2). The pattern in Figure 5b implies that high-frequency energy propagates randomly within the low-velocity zone. See Figure S2 for associated synthetics and array configurations.

3.2. Intermediate-Frequency Regime: Noise-FZ Interactions

Wavefield complexity persists at $f > f_c$ (0.5–1 Hz). ZZ correlations associated with receiver stations located within the LVZ (Figure 3b) are dominated by a longitudinally polarized arrival characterized by high apparent velocity $v_a \approx 5$ km/s. It implies that far-field *P* wave energy [*Zhang et al.*, 2009] is channeled into the FZ [*Zhang and Gerstoft*, 2014], and coherent secondary arrivals at $|\tau| \approx 3$–4 s are possibly manifestations of associated fault internal body wave reflections. Focusing on correlation fields where S_{ref} is located to the SW of the fault, fault-normal ZZ and TT moveout patterns exhibit two arrivals with $v_a \approx 5$ km/s and $v_a \approx 2.5$ km/s (Figure S5b), which propagate approximately perpendicular to the fault in NE directions. Longitudinal and circular particle motions observed in the ZR-ZZ and TR-TT planes indicate that the fast arrival is the previously identified body wave and the slow arrival a surface wave. Thus, coherent body and surface wave propagation is resolved across the velocity gradient if S_{ref} is located outside the LVZ, but the surface wave component cannot be recovered if S_{ref} is within the LVZ. This is a situation where beamforming results are relatively unstable and where data processing choices (sections 2.2 and 2.4) or subarray configurations can help resolving the superimposed wavefield components.

Considering the $v_a \approx 2.5$ km/s phase, moveout patterns associated with S_{ref} outside the LVZ exhibit time asymmetry associated with the ambient energy flux (Figure S5b). In contrast, amplitudes of correlations associated with in-fault S_{ref} locations are more symmetric, indicating increased wavefield isotropy and thus different FZ noise properties compared to the surrounding field. The increased spectral power for $f > f_c$ associated with in-fault correlations (Figure 2) is a manifestation of larger coherency within the LVZ which is ultimately controlled by better randomization of FZ noise propagation directions.

Similar to the $f < f_c$ regime, ORA rotation angles (Figures 4b and 4c) suggest surface wave excitation in SW direction, presumably along the Pacific coast. Evidence for ambient noise-FZ interaction comes from progressive alignment of propagation directions with the fault normal (Figure 4b, red) and from short-range variations within the LVZ (Figure 4c, red). This indicates that ray bending [*Roux*, 2009] can potentially bias travel time inversions in FZ environments at wavelengths comparable to the LVZ width λ_0.

3.3. High-Frequency Regime: Emergence of the Focal Spot

Surface waves at $f > 1$ Hz are characterized by wavelengths smaller than λ_0. Compared to the intermediate frequency range, stronger differences in wavefield properties within and outside the FZ indicate a transition to a different regime of noise-FZ interaction. For S_{ref} located within the LVZ (Figure 3c), TT and ZZ time-distance patterns are characterized by three features: (1) A large amplitude focal spot that quickly decreases with increasing station offset, (2) an X-shaped moveout pattern with time symmetric amplitudes within the LVZ, and (3) asymmetric arrival structure outside the LVZ. In addition, coherency across the FZ boundary is reduced compared to stations within the LVZ at similar distances (Figures S5c and S5d). It should be noted that these characteristics, notably the near-field feature (1), are best seen if amplitudes are scaled by the peak value of the correlation field. Normalizing each trace individually emphasizes the far-field properties of the pattern (Figure S5d).

Similar to the intermediate-frequency regime, the fault-normal TT and ZZ far-field X patterns consist of a $v_a \approx 0.7$ km/s slow phase exhibiting elliptical motion in the TR-TT and ZR-ZZ planes. The *P* wave associated with the longitudinally polarized arrival and $v_a \approx 5$ km/s persists in the ZZ correlations, but it is weaker compared to the situation at 0.5–1 Hz.

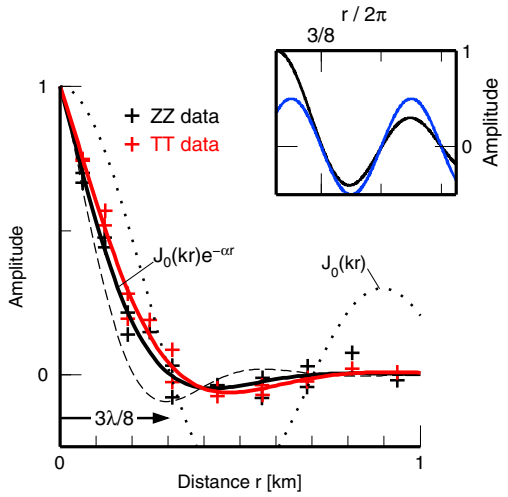

Figure 6. The shape of the 1–2 Hz focal spot emerging at $x_{ref} = -50$ m. Crosses denote measured coherency amplitudes along $\tau = 0$ s, and the solid lines are $J_0(kr)e^{-\alpha r}$ functions with best fitting k and α values. The dotted line corresponds to the corresponding undamped ZZ function, and the dashed line shows the damped function for a 50% larger k value. The wavelength can be estimated from the zero crossing of the data and the Bessel function fit. $3\lambda/8$ indicates the zero crossing of the associated ZZ Bessel function at $r = 300$ m. The inset illustrates that the Bessel function (black) and the $-\pi/4$ shifted cosine (blue) have approximately the same zero crossings, the first one at 3/8.

In-fault 2-D array beamforming at 1–2 Hz returns a speckle pattern (Figure 5b) which implies a similarly symmetric arrival time structure (feature 2) between stations characterized by bearings that are different from fault normal. It is thus the consequence of a more isotropic distribution of propagation directions within the LVZ. We verified that the pattern is not controlled by aliasing of the array response to a 1.5 Hz plane wave impinging from various directions and with different speeds, and the homogenized interstation distances (section 2.4 and Figure S2) guarantee that the focal spot does not influence the response.

Rotation angles indicate larger variability of propagation directions across the LVZ (Figures 4b and 4c, black) compared to lower frequencies. These results are associated with larger residuals due to energy on all nine components (Figure S3b), which implies a mixture of scattered surface and bulk waves.

The combined pattern of the near-field focal spot and increased in-fault amplitude symmetry is a manifestation of an isotropic surface wavefield that is spatially sampled at subwavelength intervals. These wavefield properties have long been studied in the context of time-reversal experiments [*Fink et al.*, 1989], where a pulse is emitted into a potentially heterogeneous medium that is enclosed by a virtual surface called the time-reversal mirror. If records of multiple scattered wave motion passing through this surface are time reversed and sent back into the medium, the resultant field emerging from the surface converges toward the initial source, and the time reversed beam focuses back on the source at the focal spot [*Fink*, 1997, and references therein]. The spatial focalization obtained by an active time-reversal process can be recovered using cross correlation [*Derode et al.*, 2003; *Benech et al.*, 2009], i.e., the converging, collapsing, and diverging wave can be reconstructed from the correlation field at different lapse times. In this sense, the time-distance plot (Figure 3c) represents a snapshot of the converging and diverging wavefield. The X-shaped moveout pattern is generated by propagation along the fault normal direction, and the longitudinally polarized focal spot (Figure 3f) emerges where a time-reversed wave collapses at the location of S_{ref}. The consistency between ZZ and TT results indicates that the large-amplitude feature in the ZZ pattern constitutes a focal spot and is not controlled by a possibly trapped *P* wave. A ZZ body wave focal spot can be superimposed on the reconstructed surface wave spot, but the similarity and consistency again suggest that such an interference does not govern the results.

Increased correlation time symmetry within the LVZ implies a significantly more isotropic wavefield compared to the more directional energy flux associated with asymmetric amplitudes at stations in the adjacent crust (Figure S5d). In this context, the velocity gradients bounding the LVZ can be considered as reflectors [e.g., *Ben-Zion and Aki*, 1990], which should not be confused with virtual time-reversal mirrors. Rather, the reflectors tend to trap energy inside the LVZ, which leads together with internal FZ scattering to time symmetry and improve the time-reversal performance. The resulting wavefield is similar to that trapped in a cavity, which in our case with along-strike dimension much larger than fault-normal dimension is also a FZ waveguide.

The shape of the focal spot in the space-time domain is described by the amplitude distribution $A(r)$ at $\tau = 0$ (Figure 6), where r denotes the distance between S_{ref} and receiver stations in both directions. In time-reversal experiments the shape is controlled by the symmetry properties of the wavefield and depends in the elastic case on the excitation direction of the applied force, the associated radiation pattern, and the

analyzed component of motion [*Catheline et al.*, 2008]. The distribution of the time-reversed wave energy and the focal spot shape are therefore not radial symmetric. The same principle should hold for focal spots emerging in a correlation field considering different excitation and recording components. This has not been tested experimentally, and radial symmetry cannot be assessed here due to the limited spatial sampling in directions different from fault normal. However, the observed fault normal amplitude symmetry around the location of the virtual source S_{ref} (Figure 6) constitutes a further indicator for a homogeneous intensity distribution along the direction of the linear array. Local propagation properties can be estimated from focal spots, and the smallest dimension of the refocusing spot remains of the order of half a wavelength [*Cassereau and Fink*, 1992; *Catheline et al.*, 2008; *Benech et al.*, 2009]. The experimental results allow us to estimate the fault-normal velocity structure of the LVZ cavity/waveguide from focal spot properties and to compare them to results of a travel time inversion based on far-field moveout patterns.

4. Estimates of Fault Zone Properties

4.1. Estimates From the Focal Spot

Energy focusing has been discussed in seismology in the context of amplitude enhancement through backscattering [*Larose et al.*, 2009] and passive Green's function retrieval [*Gallot et al.*, 2011], but focal spot shapes have not been inverted for estimates of medium properties as in elastography or medical imaging [*Catheline et al.*, 2008; *Brum et al.*, 2009; *Benech et al.*, 2009]. In these 3-D applications, $\lambda/2$ is estimated from the −6 dB or half width of the spot following the Rayleigh criterion, without further reference to the spot sinc function shape [*Cassereau and Fink*, 1992]. Here we are interested in a general parameterization of the amplitude (coherency) distribution $A(\tau = 0, r)$ to connect our estimates with a thorough understanding of the focal spot properties. We focus on the 1–2 Hz regime.

Considering the 2-D problem of an equipartitioned surface wavefield, the coherency $\gamma_{AB}(\omega)$ (equation (1)) is described by a Bessel function of the first kind of order zero, $J_0(kr)$, with k being the wave number ω/c [*Aki*, 1957]. Equipartitioning implies $Im[\gamma] = 0$ and hence $Re[\gamma] = J_0(kr)$, and from observing $J_0(kr) \propto Im[G_{AB}]$ [*Sánchez-Sesma and Campillo*, 2006], it follows that the time domain correlation function gives an estimate of the impulse response [*Lobkis and Weaver*, 2001]. To first order, the estimate of the band-limited inverse Fourier Transform (IFT) of the frequency domain $\gamma(\omega) = J_0(kr)e^{-\alpha r}$ indicates that the time domain focal spot shape also takes the form of an attenuated Bessel function (supporting information)

$$A(\tau = 0, r) \approx J_0(kr)e^{-\alpha r}. \tag{2}$$

We find that attenuation has to be considered to obtain reasonable fits to $A(r)$ observations (Figure 6) using equation (2), i.e., the IFT was applied to $J_0(kr)$ weighted by $e^{-\alpha r}$, with α denoting the attenuation coefficient. This approach [*Prieto et al.*, 2009] extends the original formulation associated with a homogeneous lossless medium [*Aki*, 1957]. Given the current controversy related to its validity and accuracy for noise-based attenuation estimates [e.g., *Tsai*, 2011; *Liu and Ben-Zion*, 2013; *Weaver*, 2013; *Lawrence et al.*, 2013], we focus on wave speed estimates in our discussion.

Since the focal spot is distorted by anisotropic intensity of the converging field, we fit 1–2 Hz correlation amplitudes at distances along the fault $|x| < 1.5$ km using coherency estimates limited to $r < 1$ km, which emphasizes the near-field character. The free parameters are k and α from which we estimate the phase velocity c_{focal} using $\omega = 2\pi\bar{f}$, with $\bar{f}$ the central frequency 1.5 Hz. Estimates of ZZ c_{focal} are symmetric around $x = 0$, whereas ORA-corrected T'T' results (section 2) show variations within the LVZ characterized by smaller speeds on the SW side of the fault trace compared to the NE side. For the area $0 < x < 0.5$ km, we find partially distorted focal spots and overall higher residuals (Figure S6) compared to other locations in the LVZ, which may be attributed to media changes across the fault trace and hence scatterers within the array that distort the spot shape.

In contrast to elastography applications that measure $\lambda/2$ from the spot half width, we estimate $3\lambda/8$ from the first zero crossing of the obtained distribution, which makes it insensitive to α. The factor 3/8 is related to the asymptotic approach of the Bessel function to a cosine with a phase-shifted argument by $-\pi/4$ [*Abramowitz and Stegun*, 1965, equation 9.2.1]. That is, while the zero crossing of $\cos(kr)$ is at $\pi/2 \times \lambda/2\pi$, the phase-shifted crossing occurs at $3\pi/4 \times \lambda/2\pi = 3\lambda/8$. In the example of Figure 6, $\lambda \approx 8/3 \times 0.3$ km $= 0.8$ km agrees well with the k-based estimate $\lambda = c/\bar{f} \approx 1.5$ km s/1.5 s = 1 km. This confirms that $\lambda < \lambda_0$ and supports the interpretation of cavity-like LVZ characteristics. Applying the half-width approach to the attenuation free amplitude at $J_0(kr) = 1/2$ yields a consistent estimate of $\lambda \approx 4 \times 0.2 = 0.8$ km.

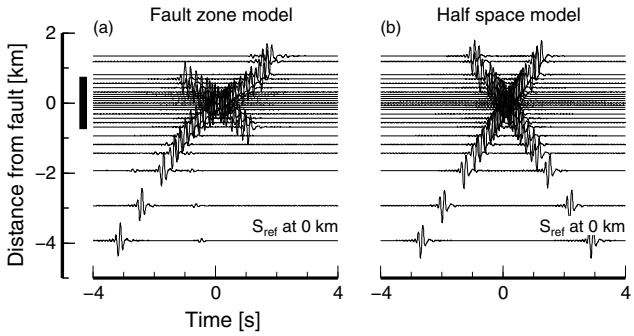

Figure 7. Synthetic correlation patterns using the Calico array station geometry. Correlations are scaled by the maximum in each time series. (a) For S_{ref} located in a 1.5 km wide low-velocity zone characterized by a 50% wave speed reduction, the arrival structure is characterized by high in-fault symmetry and anisotropic properties outside the fault, similar to observations (Figures 3c and S5d). Interstation correlations are averaged over sources that are located between [5 7] km and between [−5 − 7] km at a depth of 100 m. (b) The correlation field associated with the same source/receiver configuration in a half-space.

4.2. One-Dimensional Travel Time Inversion

The validity of the focal spot estimates can be assessed by comparison to traditional travel time results [*Catheline et al.*, 2008; *Brum et al.*, 2009; *Benech et al.*, 2009]. We compute phase (c) and group (U) velocity profiles from the arrivals that constitute the 1–2 Hz X pattern using data from all interstation correlation pairs (supporting information). Similar to the focal spot analysis, the inversion is constrained to $|x| < 1.5$ km due to difficulties in isolating high SNR arrivals across the FZ boundary. Application of the ORA improves the inversion results through arrival time shifts associated with the free realignment (ZZ→Z′Z′, TT→T′T′) in the incident wavefield, e.g., T′T′-based inversions are characterized by smaller residuals compared to TT results (Figure S7). The improvement is most significant in regions of strong velocity gradients and demonstrates the mitigation of directional propagation [*Roux*, 2009]. The results indicate that the Z′Z′ and T′T′ c and U distributions are consistent with the associated c_{focal} estimates (Figures 4d and 4e). Both methods indicate ∼50% reduced velocities in a 1–2 km wide zone and also agree on details such as the velocity variation across the fault trace (Figure 4d). Differences in the absolute values are related to the sensitivity of the inversion to the starting model (1 km/s), which implies an advantage of the focal spot method due to its independence on algorithmic choices. Overall, the compatibility of the two methods supports again their applicability and increases the confidence on the fault-normal LVZ variations resolved independently by the near- and far-field data.

5. Synthetics

To confirm further our results, we construct synthetic correlation fields that exhibit characteristic features associated with fault zone trapped noise. (The solution includes an overall velocity contrast across the fault, but this is not used here.) The synthetic calculations are based on the analytical solution of *Ben-Zion and Aki* [1990] for the scalar wavefield in a half-space with a vertical fault zone layer. The computed seismograms contain the direct wave and potential head and trapped waves for near-fault stations. The interference patterns controlling the waveform character of the FZ waves depend strongly on the width, velocity, and attenuation of the FZ layer along with propagation distance within the FZ structure [*Ben-Zion*, 1998]. The sensitivity of ballistic and scattered wavefields to FZ velocity variations alike (section 2.3) allows the application of synthetic earthquake waveforms to study first-order features of noise-FZ interaction. We compute a suite of synthetic seismograms for a model FZ structure with properties corresponding to the Calico fault environment [*Cochran et al.*, 2009] and for a homogeneous half-space model. Seismograms associated with a range of sources recorded by each station of the short-period station geometry (Figure 1b) are processed as in an earthquake waveform correlation method [*Roux and Ben-Zion*, 2013], correlated for each station pair, and source averaged.

The effect of the vertical LVZ layer on arrival time patterns is obvious when compared to synthetics generated with a homogeneous velocity structure (Figure 7). The in-fault moveout structure resembles the X pattern observed within the Calico fault (Figures 3c and S5), and the break in slope across the LVZ boundary is controlled by the imposed velocity contrast. Correlation asymmetry on both sides of the FZ is related to the lack of transparency for waves originating on the respective opposite sides. We use a dozen sources that are homogeneously distributed away from the FZ, i.e., the emerging pattern is governed by the symmetry properties of the direct arrival pattern. In this configuration, no ballistic trapped waves are generated [*Ben-Zion*, 1998] and correlated. The results highlight that features characterizing correlations of the FZ wavefield are a consequence of the symmetry properties of trapped noise propagation directions.

The reproduction of the main features associated with FZ noise suggests that an iterative reduction of correlation travel time misfits by tuning model parameters can yield estimates of FZ properties. Such a noise-based FZ imaging tool can complement analyses of trapped or reverberating ballistic waves [*Li et al.*, 1990; *Ben-Zion et al.*, 2003; *Cochran et al.*, 2009; *Lewis and Ben-Zion*, 2010; *Yang et al.*, 2011] for systematic study of FZ properties in regions of low or no seismicity.

6. Discussion and Conclusions

We developed new analysis techniques to extract high-resolution information from the ambient seismic wavefield around and within fault zone structures and demonstrated that the results are compatible with observations obtained with traditional methods based on earthquake waveforms. Moreover, certain aspects of the scattered ambient wavefield allow conclusions on properties of the low-velocity zone that augment previous interpretations based on analysis of ballistic phases.

Fault-normal velocity profiles (Figures 4d and 4e) are compatible with models based on trapped waves [*Cochran et al.*, 2009] regarding location and average velocity contrast. We emphasize that the focal spot method facilitates direct local measurements of medium properties that are compatible with traditional inversion methods. The width of the low-velocity layer is also consistent with estimates of the damage zone probed with space geodesy [*Fialko et al.*, 2002; *Fialko*, 2004]. The results provide independent confirmation of a wide compliant zone for the Calico fault with relatively small offset while demonstrating the utility of noise-based measurements in this challenging seismological situation. Constraints on the deeper parts of the fault, i.e., estimates of its dip [*Yang et al.*, 2011], are limited due to the analysis of high-frequency surface waves. The application of double-beamforming techniques offers a potential tool to focus on noise wavefield components that are sensitive to properties at deeper parts of the fault [*de Cacqueray et al.*, 2013]. The identification of a critical frequency f_c, above which the wavefield within the FZ has significantly different properties compared to the surrounding region, is also compatible with observations based on ballistic waves. Using $v \approx 1$ km/s for in-fault propagation speeds (Figures 4d and 4e), the associated wavelength $\lambda_c = v/f_c$ is about 2 km, and therefore compatible with the estimated width of the LVZ, $\lambda_c \approx \lambda_0$.

The derived geometrical and rheological properties of fault damage zones provide high-resolution information on the internal FZ structure [e.g., *Ben-Zion and Sammis*, 2003, and references therein]. This information is important for deriving accurate earthquake source properties [e.g., *Oppenheimer et al.*, 1988; *Kilb and Hardebeck*, 2006], understanding the distribution of seismic ground motion near faults [e.g., *Spudich and Olsen*, 2001; *Pischiutta et al.*, 2012; *Kurzon et al.*, 2014], and assessing likely dynamic regimes of earthquake ruptures [e.g., *Ben-Zion and Huang*, 2002; *Huang and Ampuero*, 2011; *Huang et al.*, 2014]. Local estimates of reduced elastic moduli in the FZ also constrain the rotation of background stresses [*Faulkner et al.*, 2006], which affects the mechanics during fault slip, and amplified geodetic fields [*Fialko et al.*, 2002; *Fialko*, 2004].

Noise-based methods extend the toolbox of imaging and analysis techniques targeting the interaction of fault zones and seismic wavefields, as demonstrated with the focal spot method. The Optimal Rotation Algorithm constitutes another method providing observables that can exclusively be inferred from processing of the ambient field. Results include intermediate-frequency ray bending (Figure 4b) and a significant distortion of high-frequency propagation directions within the fault (Figure 4c). These findings imply that images of FZ environments constructed from ballistic and scattered wavefields can be biased near the mechanically most interesting LVZ damage zone because of these interactions.

Our analysis techniques and results establish connections between fault zone seismology and other wave physics domains. The increased correlation time symmetry indicates the high-frequency wavefield can be considered trapped within the LVZ. The scattered in-fault wavefield is associated with efficient mixing of trapped energy, where reflections at LVZ boundaries and scattering at internal heterogeneities contribute to the randomization of incident propagation directions. This motivates the LVZ analogy with a noise cavity/waveguide for $f > f_c$, therefore providing a framework to explain specific characteristics of the wavefield. Correlation of reverberations—internal reflections related to the FZ/cavity finiteness—leads to distinct signatures [*Roux et al.*, 2008] that differ from correlations of a scattered coda or noise wavefield [*Lin et al.*, 2013; *Boué et al.*, 2013]. The lack of multiple fault-normal reflections indicates that reverberations do not dominate the correlation field, owing to data processing which minimizes the influence of earthquake signals, although the analyzed seismic energy within the LVZ may not be fully diffusive. The emergence of multiple body wave reflections in high-frequency FZ correlations [*Zhang and Gerstoft*, 2014] can likely be

tuned by data winnowing and processing choices. The cavity analogy suggests that separate processing of earthquake waveforms [*Roux and Ben-Zion*, 2013] or noise data segments [*Boué et al.*, 2014] provides an efficient strategy to image FZ structure with ballistic trapped waves and trapped noise in regions with sufficient background seismicity. Strategies enhancing in-fault reverberations from noise contribute toward monitoring the LVZ material response to perturbations [*Johnson et al.*, 2008].

The application of time-reversal concepts help understanding the emergence of the near-field focal spot and developing focal spot-based wave number estimates. The imaging approach can generally be applied in environments exhibiting properties of a cavity, e.g., low-velocity zones (this work), buildings [*Snieder and Safak*, 2006], or soft tissue phantoms [*Catheline et al.*, 2008]. The effect of refocusing also occurs in open media, e.g., in the situation of a diffuse Rayleigh wavefield propagating across the surface. The time-reversal situation associated with the reconstructed correlation field similarly requires radial symmetry of the field intensity for unbiased local measurements based on the focal spot. This constraint is related to the requirement of isotropic source or scatterer distributions for unbiased noise-based imaging [*Weaver et al.*, 2009; *Froment et al.*, 2010]. Implications of the spatial autocorrelation method [*Asten*, 2006], iterations of the correlation procedure [*Stehly et al.*, 2008], and filtering [*Gallot et al.*, 2011] can be used for bias assessment and mitigation of frequently occurring inhomogeneous intensity distributions, thus facilitating the study of local medium properties from the collapse of a time-reversed converging wavefield.

We demonstrate that properties of damage FZ layers can be estimated from synthetic correlation arrival times. This can furnish an imaging tool for investigating FZ structure that is complementary to traditional waveform modeling of ballistic FZ waves. Different theoretical solutions [*Ben-Zion and Aki*, 1990; *Ben-Zion*, 1998; *Li et al.*, 2007] combined with variable source distributions control the arrival time pattern in synthetic FZ waveforms and in the associated correlation fields that is indicative of the FZ structure. This allows systematic study of the relative contributions of source distribution, multiple reflected phases, and direct and trapped waves.

The emergence of ballistic trapped waves depends on the location and orientation of the source with respect to the trapping structure [*Ben-Zion*, 1998; *Fohrmann et al.*, 2004; *Lewis and Ben-Zion*, 2010] and on a sufficiently homogeneous waveguide between source and receiver [*Igel et al.*, 1997; *Jahnke et al.*, 2002]. Mechanisms controlling the emergence of FZ trapped noise depend only on the velocity contrast and the scattering heterogeneity and are thus more general, which provides additional possibilities for imaging internal FZ structures. Trapped noise-based tools can thus facilitate the imaging of structural properties along aseismic faults.

Acknowledgments

This work was supported by the European Research Council (Advanced grant Whisper L27507). G. Hillers acknowledges support through a Heisenberg fellowship from the German Research Foundation. Figures were made using GMT [*Wessel and Smith*, 1991]. We thank E. Cochran for providing material associated with the Calico field experiment, X. Briand for computational assistance, and S. Catheline for discussions. The manuscript benefitted from comments by D. Zigone. The facilities of the IRIS Data Management System, and specifically the IRIS Data Management Center, were used for access to waveform and metadata required in this study. Retrieval of the original seismograms from the IRIS DMS is sufficient to understand, evaluate, replicate, and build upon the reported research. The IRIS DMS is funded through the National Science Foundation and specifically the GEO Directorate through the Instrumentation and Facilities Program of the National Science Foundation under Cooperative Agreement EAR-1063471.

References

Abramowitz, M., and I. A. Stegun (Eds.) (1965), *Handbook of Mathematical Functions*, 1057 pp., Dover, New York, Constable and Company, London.

Aki, K. (1957), Space and time spectra of stationary stochastic waves, with special reference to microtremors, *Bull. Earthquake Res. Inst. Univ. Tokyo*, *35*, 415–457.

Asten, M. W. (2006), On bias and noise in passive seismic data from finite circular array data processed using SPAC methods, *Geophysics*, *71*(6), V153—V162, doi:10.1190/1.2345054.

Ben-Zion, Y. (1998), Properties of seismic fault zone waves and their utility for imaging low-velocity structure, *J. Geophy. Res.*, *103*(B6), 12,567–12,585.

Ben-Zion, Y., and K. Aki (1990), Seismic radiation from an SH line source in a laterally heterogeneous planar fault zone, *Bull. Seismol. Soc. Am.*, *80*(4), 971–994.

Ben-Zion, Y., and Y. Huang (2002), Dynamic rupture on an interface between a compliant fault zone layer and a stiffer surrounding solid, *J. Geophy. Res.*, *107*(B2), 2042, doi:10.1029/2001JB000254.

Ben-Zion, Y., and C. G. Sammis (2003), Characterization of fault zones, *Pure Appl. Geophys.*, *160*, 677–715.

Ben-Zion, Y., Z. Peng, D. Okaya, L. Seeber, J. G. Armbruster, N. Ozer, A. J. Michael, S. Baris, and M. Aktar (2003), A shallow fault zone structure illuminated by trapped waves in the Karadere-Duzce branch of the North Anatolian fault, western Turkey, *Geophys. J. Int.*, *152*, 699–717.

Benech, N., S. Catheline, J. Brum, T. Gallot, and C. A. Negreira (2009), 1-D elasticity assessment in soft solids from shear wave correlation: The time-reversal approach, *IEEE Trans. Ultrason. Ferroelectr. Freq. Control*, *56*(11), 2400–2410.

Boué, P., P. Poli, M. Campillo, H. Pedersen, X. Briand, and P. Roux (2013), Teleseismic correlations of ambient seismic noise for deep global imaging of the Earth, *Geophys. J. Int.*, *194*, 844–848, doi:10.1093/gji/ggt160.

Boué, P., P. Poli, M. Campillo, and P. Roux (2014), Reverberations, coda waves and ambient noise: Correlations at the global scale and retrieval of the deep phases, *Earth Planet. Sci. Lett.*, *391*, 137–145, doi:10.1016/j.epsl.2014.01.047.

Brum, J., S. Catheline, N. Benech, and C. Negreira (2009), Shear elasticity estimation from surface wave: The time reversal approach, *J. Acoust. Soc. Am.*, *124*(6), 3377–3380, doi:10.1121/1.2998769.

Campillo, M. (2006), Phase and correlation of "random" seismic fields and the reconstruction of the Green function, *Pure Appl. Geophys.*, *163*, 475–502, doi:10.1007/s00024-005-0032-8.

Cassereau, D., and M. Fink (1992), Time-reversal of ultrasonic fields—Part III: Theory of the closed time-reversal cavity, *IEEE Trans. Ultrason. Ferroelectr. Freq. Control*, *39*(5), 579–592.

Catheline, S., N. Benech, J. Brum, and C. Negreira (2008), Time reversal of elastic waves in soft solids, *Phys. Rev. Lett.*, *100*(6), 064301, doi:10.1103/PhysRevLett.100.064301.

Cochran, E. S., Y.-G. Li, P. M. Shearer, S. Barbot, Y. Fialko, and J. E. Vidale (2009), Seismic and geodetic evidence for extensive, long-lived fault damage zones, *Geology*, *37*(4), 315–318, doi:10.1130/G25306A.1.

de Cacqueray, B., P. Roux, M. Campillo, and S. Catheline (2013), Tracking of velocity variations at depth in the presence of surface velocity fluctuations, *Geophysics*, *78*(1), U1—U8, doi:10.1190/GEO2010-0071.1.

Derode, A., A. Tourin, and M. Fink (2001), Random multiple scattering of ultrasound. II. Is time reversal a self-averaging process?, *Phys. Rev. E*, *64*, 036606, doi:10.1103/PhysRevE.64.036606.

Derode, A., E. Larose, M. Campillo, and M. Fink (2003), How to estimate the Green's function of a heterogeneous medium between two passive sensors? Application to acoustic waves, *Appl. Phys. Lett.*, *83*(15), 3054–3056, doi:10.1063/1.1617373.

Faulkner, D. R., T. M. Mitchell, D. Healy, and M. J. Heap (2006), Slip on "weak" faults by the rotation of regional stress in the fracture damage zone, *Nature*, *444*, 922–925, doi:10.1038/nature05353.

Fialko, Y. (2004), Probing the mechanical properties of seismically active crust with space geodesy: Study of coseismic deformation due to the 1992 M_w7.3 Landers (Southern California) earthquake, *J. Geophy. Res.*, *109*, B03307, doi:10.1029/2003JB002756.

Fialko, Y., D. Sandwell, D. Agnew, M. Simons, P. Shearer, and B. Minster (2002), Deformation on nearby faults induced by the 1999 Hector Mine earthquake, *Science*, *297*, 1858–1862, doi:10.1126/science.1074671.

Fink, M. (1997), Time reversed acoustics, *Phys. Today*, *50*(3), 34–40, doi:10.1063/1.881692.

Fink, M., C. Prada, F. Wu, and D. Cassereau (1989), Self-focusing in inhomogeneous media with time-reversal acoustic mirrors, *Proc. IEEE Ultrason. Symp.*, *2*, 681–686.

Fohrmann, M., H. Igel, G. Jahnke, and Y. Ben-Zion (2004), Guided waves from sources outside faults: An indication for shallow fault zone structure?, *Pure Appl. Geophys.*, *161*, 2125–2137, doi:10.1007/s00024-004-2553-y.

Froment, B., M. Campillo, P. Roux, P. Gouédard, A. Verdel, and R. L. Weaver (2010), Estimation of the effect of nonisotropically distributed energy on the apparent arrival time in correlations, *Geophysics*, *75*(5), 85–93, doi:10.1190/1.3483102.

Gallot, T., S. Catheline, P. Roux, and M. Campillo (2011), A passive inverse filter for Green's function retrieval, *J. Acoust. Soc. Am.*, *131*(1), EL21–EL27, doi:10.1121/1.3665397.

Gerstoft, P., and T. Tanimoto (2007), A year of microseisms in Southern California, *Geophys. Res. Lett.*, *34*, L20304, doi:10.1029/2007GL031091.

Hennino, R., N. Trégourès, N. M. Shapiro, L. Margerin, M. Campillo, B. A. van Tiggelen, and R. L. Weaver (2001), Observation of equipartitioning of seismic waves, *Phys. Rev. Lett.*, *86*(15), 3447–3450, doi:10.1103/PhysRevLett.86.3447.

Hillers, G., M. Campillo, Y.-Y. Lin, K.-F. Ma, and P. Roux (2012), Anatomy of the high-frequency ambient seismic wave field at the TCDP borehole, *J. Geophy. Res.*, *117*, B06301, doi:10.1029/2011JB008999.

Hillers, G., Y. Ben-Zion, M. Landès, and M. Campillo (2013), Interaction of microseisms with crustal heterogeneity: A case study from the San Jacinto fault zone area, *Geochem. Geophys. Geosyst.*, *14*(7), 2182–2197, doi:10.1002/ggge.20140.

Hillers, G., M. Campillo, and K.-F. Ma (2014), Seismic velocity variations at TCDP are controlled by MJO driven precipitation pattern and high fluid discharge properties, *Earth Planet. Sci. Lett.*, *391*, 121–127, doi:10.1016/j.epsl.2014.01.040.

Hong, T.-K., and W. Menke (2006), Tomographic investigation of the wear along the San Jacinto fault, Southern California, *Phys. Earth Planet. Inter.*, *155*, 236–248.

Huang, Y., and J.-P. Ampuero (2011), Pulse-like ruptures induced by low-velocity fault zones, *J. Geophy. Res.*, *116*, B12307, doi:10.1029/2011JB008684.

Huang, Y., J.-P. Ampuero, and D. V. Helmberger (2014), Earthquake ruptures modulated by waves in damaged fault zones, *J. Geophy. Res.*, *119*, 3133–3154, doi:10.1002/2013JB010724.

Igel, H., Y. Ben-Zion, and P. C. Leary (1997), Simulation of SH- and P-SV-wave propagation in fault zones, *Geophys. J. Int.*, *128*, 533–546.

Jahnke, G., H. Igel, and Y. Ben-Zion (2002), Three-dimensional calculations of fault-zone-guided waves in various irregular structures, *Geophys. J. Int.*, *151*, 416–426.

Johnson, P. A., H. Savage, M. Knuth, J. Gomberg, and C. Marone (2008), Effects of acoustic waves on stick-slip in granular media and implications for earthquakes, *Nature*, *451*, 57–60, doi:10.1038/nature06440.

Kilb, D., and J. L. Hardebeck (2006), Fault parameter constraints using relocated earthquakes: A validation of first-motion focal-mechanism data, *Bull. Seismol. Soc. Am.*, *96*(3), 1140–1158.

Kurzon, I., F. L. Vernon, Y. Ben-Zion, and G. Atkinson (2014), Ground motion prediction equations in the San Jacinto Fault Zone—Significant effects of rupture directivity and fault zone amplification, *Pure Appl. Geophys.*, *171*, doi:10.1007/s00024-014-0855-2.

Landès, M., F. Hubans, N. M. Shapiro, A. Paul, and M. Campillo (2010), Origin of deep ocean microseisms by using teleseismic body waves, *J. Geophy. Res.*, *115*, B05302, doi:10.1029/2009JB006918.

Larose, E., L. Margerin, B. A. van Tiggelen, and M. Campillo (2009), Weak localization of seismic waves, *Phys. Rev. Lett.*, *93*(4), 048501, doi:10.1103/PhysRevLett.93.048501.

Lawrence, J. F., M. Denolle, K. J. Seats, and G. A. Prieto (2013), A numeric evaluation of attenuation from ambient noise correlation functions, *J. Geophy. Res. Solid Earth*, *118*, 6134–6145, doi:10.1002/2012JB009513.

Lewis, M. A., and Y. Ben-Zion (2010), Diversity of fault zone damage and trapping structures in the Parkfield section of the San Andreas fault from comprehensive analysis of near fault seismograms, *Geophys. J. Int.*, *183*, 1579–1595, doi:10.1111/j.1365-246X.2010.04816.x.

Li, H., L. Zhu, and H. Yang (2007), High-resolution structures of the Landers fault zone inferred from aftershock waveform data, *Geophys. J. Int.*, *171*, 1295–1307, doi:10.1111/j.1365-246X.2007.03608.x.

Li, Y.-G., P. Leary, K. Aki, and P. Malin (1990), Seismic trapped modes in the oroville and San Andreas fault zones, *Science*, *249*(4970), 763–766, doi:10.1126/science.249.4970.763.

Lin, F.-C., V. C. Tsai, B. Schmandt, Z. Duputel, and Z. Zhan (2013), Extracting seismic core phases with array interferometry, *Geophys. Res. Lett.*, *40*, 1049–1053, doi:10.1002/grl.50237.

Liu, X., and Y. Ben-Zion (2013), Theoretical and numerical results on effects of attenuation on correlation functions of ambient seismic noise, *Geophys. J. Int.*, *194*, 1966–1983, doi:10.1093/gji/ggt215.

Lobkis, O. I., and R. L. Weaver (2001), On the emergence of the Green's function in the correlations of a diffuse field, *J. Acoust. Soc. Am.*, *110*(6), 3011–3017.

Margerin, L., M. Campillo, B. A. van Tiggelen, and R. Hennino (2009), Energy partition of seismic coda waves in layered media: Theory and application to Pinyon Flats Observatory, *Geophys. J. Int.*, *177*, 571–585, doi:10.1111/j.1365-246X.2008.04068.x.

Oppenheimer, D. H., P. A. Reasenberg, and R. W. Simpson (1988), Fault plane solutions for the 1984 Morgan Hill, California, earthquake sequence: Evidence for the state of stress on the Calaveras fault, *J. Geophy. Res.*, *93*, 9007–9026.
Pischiutta, M., F. Salvini, J. Fletcher, A. Rovelli, and Y. Ben-Zion (2012), Horizontal polarization of ground motion in the Hayward fault zone at Fremont, California: Dominant fault-high-angle polarization and fault-induced cracks, *Geophys. J. Int.*, *188*, 1255–1272, doi:10.1111/j.1365-246X.2011.05319.x.
Poli, P., M. Campillo, H. A. Pedersen, and LAPNET Working Group (2012a), Body-wave imaging of Earth's mantle discontinuities from ambient seismic noise, *Science*, *338*, 1063–1065, doi:10.1126/science.1228194.
Poli, P., H. A. Pedersen, M. Campillo, and POLENET/LAPNET Working Group (2012b), Emergence of body waves from cross-correlation of short period seismic noise, *Geophys. J. Int.*, *188*, 549–558, doi:10.1111/j.1365-246X.2011.05271.x.
Poli, P., H. A. Pedersen, M. Campillo, and POLENET/LAPNET Working Group (2013), Noise directivity and group velocity tomography in a region with small velocity contrasts: The northern Baltic shield, *Geophys. J. Int.*, *192*, 413–424, doi:10.1093/gji/ggs034.
Prieto, G. A., J. F. Lawrence, and G. C. Beroza (2009), Anelastic Earth structure from the coherency of the ambient seismic field, *J. Geophy. Res.*, *114*, B07303, doi:10.1029/2008JB006067.
Roux, P. (2009), Passive seismic imaging with direct ambient noise: Application to surface waves and the San Andreas fault in Parkfield, CA, *Geophys. J. Int.*, *179*, 367–373, doi:10.1111/j.1365-246X.2009.04282.x.
Roux, P., and Y. Ben-Zion (2013), Monitoring fault zone environments with correlations of earthquake waveforms, *Geophys. J. Int.*, *196*, 1073–1081, doi:10.1093/gji/ggt441.
Roux, P., K. G. Sabra, P. Gerstoft, W. A. Kuperman, and M. C. Fehler (2005), P-waves from cross-correlation of seismic noise, *Geophys. Res. Lett.*, *32*, L19303, doi:10.1029/2005GL023803.
Roux, P., B. D. Cornuelle, W. A. Kuperman, and W. S. Hodgkiss (2008), The structure of raylike arrivals in a shallow-water waveguide, *J. Acoust. Soc. Am.*, *124*(6), 3430–3439, doi:10.1121/1.2996330.
Sánchez-Sesma, F. J., and M. Campillo (2006), Retrieval of the Green's function from cross correlation: The canonical elastic problem, *Bull. Seismol. Soc. Am.*, *96*(3), 1182–1191, doi:10.1785/0120050181.
Sánchez-Sesma, F. J., M. Rodríguez, U. Iturrarán-Viveros, F. Luzón, M. Campillo, L. Margerin, A. García-Jerez, M. Suarez, M. A. Santoyo, and A. Rodríguez-Castellanos (2011), A theory for microtremor h/v spectral ratio: Application for a layered medium, *Geophys. J. Int.*, *186*, 221–225, doi:10.1111/j.1365-246X.2011.05064.x.
Scheingraber, C., K. Hosseini, R. Barsch, and K. Sigloch (2013), ObsPyLoad: A tool for automated retrieval of seismological waveform data, *Seism. Res. Let.*, *84*(3), 525–531, doi:10.1785/0220120103.
Schulte-Pelkum, V., P. S. Earle, and F. L. Vernon (2004), Strong directivity of ocean-generated seismic noise, *Geochem. Geophys. Geosyst.*, *5*(3), Q03004, doi:10.1029/2003GC000520.
Shapiro, N. M., M. Campillo, L. Margerin, S. K. Singh, V. Kostoglodov, and J. Pacheco (2000), The energy partitioning and the diffuse character of the seismic coda, *Bull. Seismol. Soc. Am.*, *90*(3), 655–665.
Shapiro, N. M., M. Campillo, L. Stehly, and M. H. Ritzwoller (2005), High-resolution surface-wave tomography from ambient seismic noise, *Science*, *307*, 1615–1618, doi:10.1126/science.1108339.
Snieder, R., and E. Safak (2006), Extracting the building response using seismic interferometry: Theory and application to the Millikan Library in Pasadena, California, *Bull. Seismol. Soc. Am.*, *96*(2), 586–598, doi:10.1785/0120050109.
Spudich, P., and K. B. Olsen (2001), Fault zone amplified waves as a possible seismic hazard along the Calaveras fault in central California, *Geophys. Res. Lett.*, *28*, 2533–2536.
Stehly, L., M. Campillo, and N. M. Shapiro (2006), A study for the seismic noise from its long-range correlation properties, *J. Geophy. Res.*, *111*, B10306, doi:10.1029/2005JB004237.
Stehly, L., M. Campillo, B. Froment, and R. L. Weaver (2008), Reconstructing Green's function by correlation of the coda of the correlation (C^3) of ambient seismic noise, *J. Geophy. Res.*, *113*, B11306, doi:10.1029/2008JB005693.
Stehly, L., B. Fry, M. Campillo, N. M. Shapiro, J. Guilbert, L. Boschi, and D. Giardini (2009), Tomography of the Alpine region from observations of seismic ambient noise, *Geophys. J. Int.*, *178*, 338–350, doi:10.1111/j.1365-246X.2009.04132.x.
Tsai, V. C. (2011), Understanding the amplitudes of noise correlation measurements, *J. Geophy. Res.*, *116*, B09311, doi:10.1029/2011JB008483.
Vandemeulebrouck, J., R. Roux, P. Gouédard, A. Legaz, A. Revil, A. W. Hurst, A. Bolève, and A. Jardani (2009), Application of acoustic noise and self-potential localization techniques to a buried hydrothermal vent (Waimangu Old Geyser site, New Zealand), *Geophys. J. Int.*, *180*, 883–890, doi:10.1111/j.1365-246X.2009.04454.x.
Verbeke, J., L. Boschi, L. Stehly, E. Kissling, and A. Michelini (2012), High-resolution Rayleigh-wave velocity maps of central Europe from a dense ambient-noise data set, *Geophys. J. Int.*, *188*, 1173–1187, doi:10.1111/j.1365-246X.2011.05308.x.
Wagner, G. S. (1998), Local wave propagation near the San Jacinto fault zone, Southern California: Observations from a three-component seismic array, *J. Geophy. Res.*, *103*(B4), 7231–7246.
Weaver, R. L. (1982), On diffuse waves in solid media, *J. Acoust. Soc. Am.*, *71*(6), 1608–1609.
Weaver, R. L. (2013), On the retrieval of attenuation and site amplification from ambient noise on linear arrays: Further numerical simulations, *Geophys. J. Int.*, *193*, 1644–1657, doi:10.1093/gji/ggt063.
Weaver, R. L., B. Froment, and M. Campillo (2009), On the correlation of non-isotropically distributed ballistic scalar diffuse waves, *J. Acoust. Soc. Am.*, *126*(4), 1817–1826, doi:10.1121/1.3203359.
Wegler, U. (2003), Analysis of multiple scattering at Vesuvius volcano, Italy, using data of the TomoVes active seismic experiment, *J. Volcanol. Geotherm. Res.*, *128*, 45–63, doi:10.1016/S0377-0273(03)00246-4.
Wessel, P., and W. H. F. Smith (1991), Free software helps map and display data, *Eos Trans. AGU*, *72*(41), 441–446.
Yang, H., L. Zhu, and E. S. Cochran (2011), Seismic structures of the Calico fault zone inferred from local earthquake travel time modelling, *Geophys. J. Int.*, *186*, 760–770, doi:10.1111/j.1365-246X.2011.05055.x.
Zhang, J., and P. Gerstoft (2014), Local-scale cross-correlation of seismic noise from the Calico fault experiment, *Earthquake Sci.*, doi:10.1007/s11589-014-0074-z.
Zhang, J., P. Gerstoft, and P. M. Shearer (2009), High-frequency P-wave seismic noise driven by ocean winds, *Geophys. Res. Lett.*, *36*, L09302, doi:10.1029/2009GL037761.
Zigone, D., Y. Ben-Zion, M. Campillo, and P. Roux (2014), Seismic Tomography of the Southern California plate boundary region from noise-based Rayleigh and Love waves, *Pure Appl. Geophys.*, doi:10.1007/s00024-014-0872-1.

Supplementary material to: Seismic fault zone trapped noise

Gregor Hillers[1*], Michel Campillo[1], Yehuda Ben-Zion[2], and Philippe Roux[1]

[1]Institut des Sciences de la Terre, Université Joseph Fourier, Grenoble, France
[2]Department of Earth Sciences, University of Southern California, Los Angeles, USA

[*]To whom correspondence should be addressed; E-mail: gregor.hillers@ujf-grenoble.fr

The supplementary figures in this document

are ordered along the discussion in the main text.

Data Processing

'Long-Range' and 'Short-Range' Estimates from the Optimal Rotation Algorithm (ORA)

Results of the ORA (Fig. S3) applied to the fault normal broadband data are visualized using three matrices (Fig. S4), where the full $\mathbf{M}^{\Psi}_{ij}$ matrix (Fig. S4a) displays angles Ψ_{A}, Ψ_{B} associated with a station pair A, B on either side of the diagonal, $\mathbf{M}^{-}_{ij}$ contains the difference $\Psi_{\mathrm{A}} - \Psi_{\mathrm{B}}$ (Fig. S4b), and $\mathbf{M}^{r}_{ij}$ the associated residual (Fig. S4c). To synthesize the information contained in these images we construct average azimuth profiles (main text Figs. 4b, c). For each station (indexed i) we compute an average angle $\overline{\psi} = \sum \mathbf{\Psi}\mathbf{w} / \sum \mathbf{w}$ using the vectors $\mathbf{\Psi} = [\mathbf{M}^{\Psi}_{i,j=1\ldots n}\, \mathbf{M}^{\Psi}_{i=1\ldots n,j}]$ (all values in row i and column $j = i$) and the weights $\mathbf{w} = [\mathbf{M}^{r}_{i,j=1\ldots n}\, \mathbf{M}^{r}_{i,j=1\ldots n}]$. The duplication is necessary because each Ψ_{A}, Ψ_{B} is associated with one residual. Note that no values are available for $j = i$. This realization yields a long-range estimate, because the residuals increase with station distance. A corresponding short-range estimate emphasizes values around the diagonal using $\mathbf{w} = [\mathbf{M}^{r}_{i,j=1\ldots n}\, \mathbf{M}^{r}_{i,j=1\ldots n}]^{-1}$.

Velocity Estimates

Focal Spot Method

We estimate the functional form of the near field amplitude distribution $A(r)$ in the time domain along zero correlation lag time to fit amplitude data for the imaging of local wave propagation parameters. The resolution of the focal spot (main text Figure 6) is a consequence of the dense spatial sampling in the fault-normal direction compared to

wave length at which the isotropic noise is trapped in the LVZ cavity. We discuss the present 2-D surface wave problem together with the 3-D case associated with applications in elastography [*Catheline et al.*, 2008], where it has been demonstrated that velocity variations within a soft tissue substitute can be imaged using focal spot properties. The Fourier domain Green's functions in two and three dimension are [e.g., *Snieder*, 2009]

$$G^{2\mathrm{D}}(r) = \frac{-i}{4} H_0^{(1)}(kr) \quad \text{and} \tag{1}$$

$$G^{3\mathrm{D}}(r) = \frac{-1}{4\pi} \frac{e^{ikr}}{r}, \tag{2}$$

where $H_0^{(1)}$ is the first Hankel function of degree zero, k is the wave number satisfying $k = \omega/c$, and r is the source-receiver distance, or, in the context of noise correlations, the inter-station distance. The 2-D equation is synonymous with the notation of *Sánchez-Sesma and Campillo* [2006] considering different FT definitions and that the Hankel function is a linear combination of the Bessel function J_0 and the Neumann function Y_0

$$G^{2\mathrm{D}}(r) = -\frac{1}{4\mu} \left[Y_0(kr) + iJ_0(kr) \right]. \tag{3}$$

Considering attenuation, the terms in brackets $[\cdot]$ is weighted by $e^{-\alpha r}$ [*Prieto et al.*, 2009; *Lawrence et al.*, 2013], where α is the attenuation coefficient, which is related to the Q factor via frequency f and group velocity U as $\alpha = \pi f/UQ$. The connection between Equation 3 and the complex coherency $\gamma_{\mathrm{AB}}(\omega)$ (main text Equation 1) is the basis of Aki's SPAC method [*Aki*, 1957], who showed that the spatial correlation of two wave fields at A and B takes the form of a Bessel function, $\gamma_{\mathrm{AB}}(\omega) = J_0(kr)$. The consistency between the SPAC method and time domain correlations has been demonstrated for equipartitioned wave fields [*Yokoi and Margaryan*, 2008], for which $Im[\gamma] = 0$ [*Asten*, 2006], yielding $Re[\gamma] = J_0(kr)$. Hence, the coherency is described by the Bessel function, i.e., the imaginary part of the Green's function, $J_0(kr) \propto Im[G_{\mathrm{AB}}]$ [*Sánchez-Sesma and*

Campillo, 2006], showing that the time domain correlation function is a practitioners estimate of the impulse response. Because we are interested in the functional form of the shape of the amplitude (coherency) distribution along zero lag time $\tau = 0$, we must take $A(t = 0, r) = IFT[\gamma]$ [see also Appendix of *Prieto et al.*, 2009] under the assumption of isotropy ($\gamma = J_0(kr)e^{-\alpha r}$)

$$\begin{aligned} A(t=0,r) &= \int_{-\infty}^{\infty} J_0(kr)e^{-\alpha r}e^{i\omega t}d\omega \\ &\approx \int_{\omega_0-\Delta\omega}^{\omega_0+\Delta\omega} J_0(k_0 r)e^{-\alpha r}d\omega \\ &\approx J_0(k_0 r)e^{-\alpha r}, \end{aligned} \tag{4}$$

neglecting higher order terms, replacing τ by t, and $k_0 = \omega_0/c$. In practice, $\omega_0 = 2\pi\overline{f}$, where $\overline{f}$ is the central frequency of a band limited representation of γ, i.e., whitening is performed in the frequency band $[\omega_0 - \Delta\omega,\ \omega_0 + \Delta\omega]$. The consistency of our $A(r)$ measurements with Equation 4 (main text Figure 6) suggests that discounting higher order terms is an acceptable approximation for the present purpose of demonstrating the applicability of the near-field method in a challenging seismological situation. The generality of these statements should be tested using data from dense 2-D arrays [*Gouédard et al.*, 2008; *Gallot et al.*, 2011; *Lin et al.*, 2013] to investigate the sensitivity of the approach to heterogeneous azimuthal averaging in the presence of non-uniform propagation directions, and to explore the applicability of techniques that mitigate wave field directivity [*Gallot et al.*, 2011].

Because of the simpler form of the Green's function in the full space (Eq. 1) the shape of the focal spot in 3-D corresponding to Equation 4 is described by a sinc function [*Cassereau and Fink*, 1992]. In attenuation free situations, the wave length λ can directly be estimated from the focal spot half or -6-dB width Δr [*Cassereau and Fink*, 1992; *Catheline et al.*, 2008; *Benech et al.*, 2009]. For motion along the 'recording' or

'observation' direction $\Delta r \approx \lambda$, whereas for orthogonal motion $\Delta r \approx \lambda/2$. The accuracy of the estimate depends on the compatibility of the experimental configuration with the theoretical model, and on spectral properties of the wave field.

Equation 4 may still be inaccurate for estimates of the attenuation coefficient. The situation of an attenuated Bessel function holds for isotropic far field sources, whereas coherency functions associated with more complex Q structures and source distributions are described by more complicated expressions [*Tsai*, 2011; *Liu and Ben-Zion*, 2013; *Weaver*, 2013]. The validity of the resulting fault-normal α profile (Fig. S6b) has to be verified in future studies considering variable inter-station attenuation, network-internal secondary sources in form of scatterers, and site effects.

The attenuation profile is characterized by a fault-normal inverse velocity dependence, and thus compatible with the general observation of increased amplitude damping in compliant fault damage zones. Interestingly, the distribution of the three observables displayed in Figure S6 (c_{focal}, α, scaled regression-error) show a sensitivity to properties between $x = 0$ and $x = 200$ m. Similar fluctuations in the same region can be extracted from the rotation azimuths (main text Figs. 4b, c), in addition to the velocity variations suggested by the TT c and U profiles (main text Fig. 4d, Fig. S7). Together with the consistent estimates of FZ position and width, and spatial variations of the H^2/V^2 spectral ratios, our results suggest that the focal spot method provides independent observations for consistency-checks.

Phase Method / Fault-Normal 1-D Travel Time Inversion

We invert fault-normal group (U) and phase (c) velocity profiles from all inter-station correlation U and c surface wave arrival time estimates. First, we compute a Green's function estimate G from the band-limited correlation function C using $G(\tau) = -dC(\tau)/d\tau$, con-

struct an average of the causal and acausal part, compute the envelope, and associate the timing of the maximum amplitude with a group velocity arrival time t^U. For estimates of t^c, we multiply the τ-symmetric G with a Gaussian window centered on t^U, take the Fourier Transform, add $\pi/4$ to the phase ϕ, unwrap the phase, and get $t^c = \phi(\omega)/\omega + \Delta\tau$. For the 1–2 Hz data, $\omega = 2\pi\overline{f}$, with $\overline{f} = 1.5$ Hz (associated with the Gaussian taper); $\Delta\tau$ is the maximum time lag of $G(\tau)$ (e.g., 30 s).

We consider only estimates in the inversion that do not interfere with the large amplitude focal spot, which biases an accurate determination of surface wave arrivals at short inter-station distances. The forward problem consists of the linear combinations $t_i = \sum_{j=1}^{n-1} d_{ij} s_j$, where $t_i^{U,c}$ are the independent pair-wise travel time measurements, s_j denote the slowness estimates between each neighbored station pair, and d_{ij} is the matrix that contains the weighted inter-station distances. The number of stations is n. Representing the problem in the general form $\mathbf{d} = \mathbf{Gm}$ ($\mathbf{d} = t_i$, $\mathbf{G} = d_{ij}$, $\mathbf{m} = s_j$), the inverse problem of this overdetermined system is solved using

$$\mathbf{m} = \mathbf{m_0} + \left(\mathbf{G}^T\mathbf{C}_d\mathbf{G} + \mathbf{C}_m\right)^{-1}\mathbf{G}^T{\mathbf{C}_d}^{-1}\left(\mathbf{d} - \mathbf{G}\mathbf{m}_0\right), \tag{5}$$

where $\mathbf{m}_0$ is the starting model, $\mathbf{G}^T$ the transposed of $\mathbf{G}$, and $\mathbf{C}_m$ and $\mathbf{C}_d$ are the model and data covariance matrices, respectively. For a given station pair separated by r we use $C_m = (\sigma\lambda_0/\lambda)^2 \exp(-r/\lambda)$, where σ and λ are slowness and spatial smoothing parameters, λ_0 is the cell size or inter-station distance (λ, λ_0 should not be confused with wavelength and FZ width). The solution is sensitive to choices of $\mathbf{C}_d$ (e.g., constant weights; SNR-dependent weights; the range of values obtained from dt measurements at negative or positive time lags, compared to the lag-time averaged correlation), to λ_0 (the spatial discretization is heterogeneous), and to the starting model $\mathbf{m}_0$ (here: 1 km/s).

References

Aki, K. (1957), Space and time spectra of stationary stochastic waves, with special reference to microtremors, *Bull. Earthquake Res. Inst. Univ. Tokyo*, *35*, 415–457.

Asten, M. W. (2006), On bias and noise in passive seismic data from finite circular array data processed using SPAC methods, *Geophysics*, *71*(6), V153–V162, doi: 10.1190/1.2345054.

Benech, N., S. Catheline, J. Brum, T. Gallot, and C. A. Negreira (2009), 1-D Elasticity Assessment in Soft Solids from Shear Wave Correlation: The Time-Reversal Approach, *IEEE Trans. Ultrason. Ferroelectr. Freq. Control*, *56*(11), 2400–2410.

Cassereau, D., and M. Fink (1992), Time-Reversal of Ultrasonic Fields—Part III: Theory of the Closed Time-Reversal Cavity, *IEEE Trans. Ultrason. Ferroelectr. Freq. Control*, *39*(5), 579–592.

Catheline, S., N. Benech, J. Brum, and C. Negreira (2008), Time Reversal of Elastic Waves in Soft Solids, *Phys. Rev. Lett.*, *100*(6), 064,301, doi:10.1103/PhysRevLett.100.064301.

Cochran, E. S., Y.-G. Li, P. M. Shearer, S. Barbot, Y. Fialko, and J. E. Vidale (2009), Seismic and geodetic evidence for extensive, long-lived fault damage zones, *Geology*, *37*(4), 315–318, doi:10.1130/G25306A.1.

Gallot, T., S. Catheline, P. Roux, and M. Campillo (2011), A passive inverse filter for Green's function retrieval, *J. Acoust. Soc. Am.*, *131*(1), EL21–EL27, doi: 10.1121/1.3665397.

Gouédard, P., P. Roux, M. Campillo, and A. Verdel (2008), Convergence of the two-point

correlation function toward the Green's function in the context of a seismic-prospecting data set, *Geophysics*, *73*(6), 47–53, doi:10.1190/1.2985822.

Lawrence, J. F., M. Denolle, K. J. Seats, and G. A. Prieto (2013), A numeric evaluation of attenuation from ambient noise correlation functions, *J. Geophy. Res.*, *118*, doi: 10.1002/2012JB009513.

Lin, F.-C., D. Li, R. W. Clayton, and D. Hollis (2013), High-resolution 3D shallow crustal structure in Long Beach, California: Application of ambient noise tomography on a dense seismic array, *Geophysics*, *78*(4), Q45–Q56, doi:10.1190/GEO2012-0453.1.

Liu, X., and Y. Ben-Zion (2013), Theoretical and numerical results on effects of attenuation on correlation functions of ambient seismic noise, *Geophys. J. Int.*, *194*, 1966–1983, doi:10.1093/gji/ggt215.

Prieto, G. A., J. F. Lawrence, and G. C. Beroza (2009), Anelastic Earth structure from the coherency of the ambient seismic field, *J. Geophy. Res.*, *114*(B07303), doi: 10.1029/2008JB006067.

Roux, P. (2009), Passive seismic imaging with direct ambient noise: application to surface waves and the San Andreas Fault in Parkfield, CA, *Geophys. J. Int.*, *179*, 367–373, doi: 10.1111/j.1365-246X.2009.04282.x.

Sánchez-Sesma, F. J., and M. Campillo (2006), Retrieval of the Green's Function from Cross Correlation: The Canonical Elastic Problem, *Bull. Seism. Soc. Am.*, *96*(3), 1182–1191, doi:10.1785/0120050181.

Snieder, R. (Ed.) (2009), *A Guided Tour of Mathematical Methods for the Physical Sciences*, 2nd ed., 57 pp., Cambridge University Press, Cambridge.

Tsai, V. C. (2011), Understanding the amplitudes of noise correlation measurements, *J. Geophy. Res.*, *116*, B09311, doi:10.1029/2011JB008483.

Weaver, R. L. (2013), On the retrieval of attenuation and site amplification from ambient noise on linear arrays: further numerical simulations, *Geophys. J. Int.*, *193*, 1644–1657, doi:10.1093/gji/ggt063.

Yokoi, T., and S. Margaryan (2008), Consistency of the spatial autocorrelation method with seismic interferometry and its consequence, *Geophysical Prospecting*, *56*, 435–451, doi:10.1111/j.1365-2478.2008.00709.x.

Zhang, J., and P. Gerstoft (2014), Local-scale cross-correlation of seismic noise from the Calico fault experiment, *Earthq. Sci.*, doi:10.1007/s11589-014-0074-z.

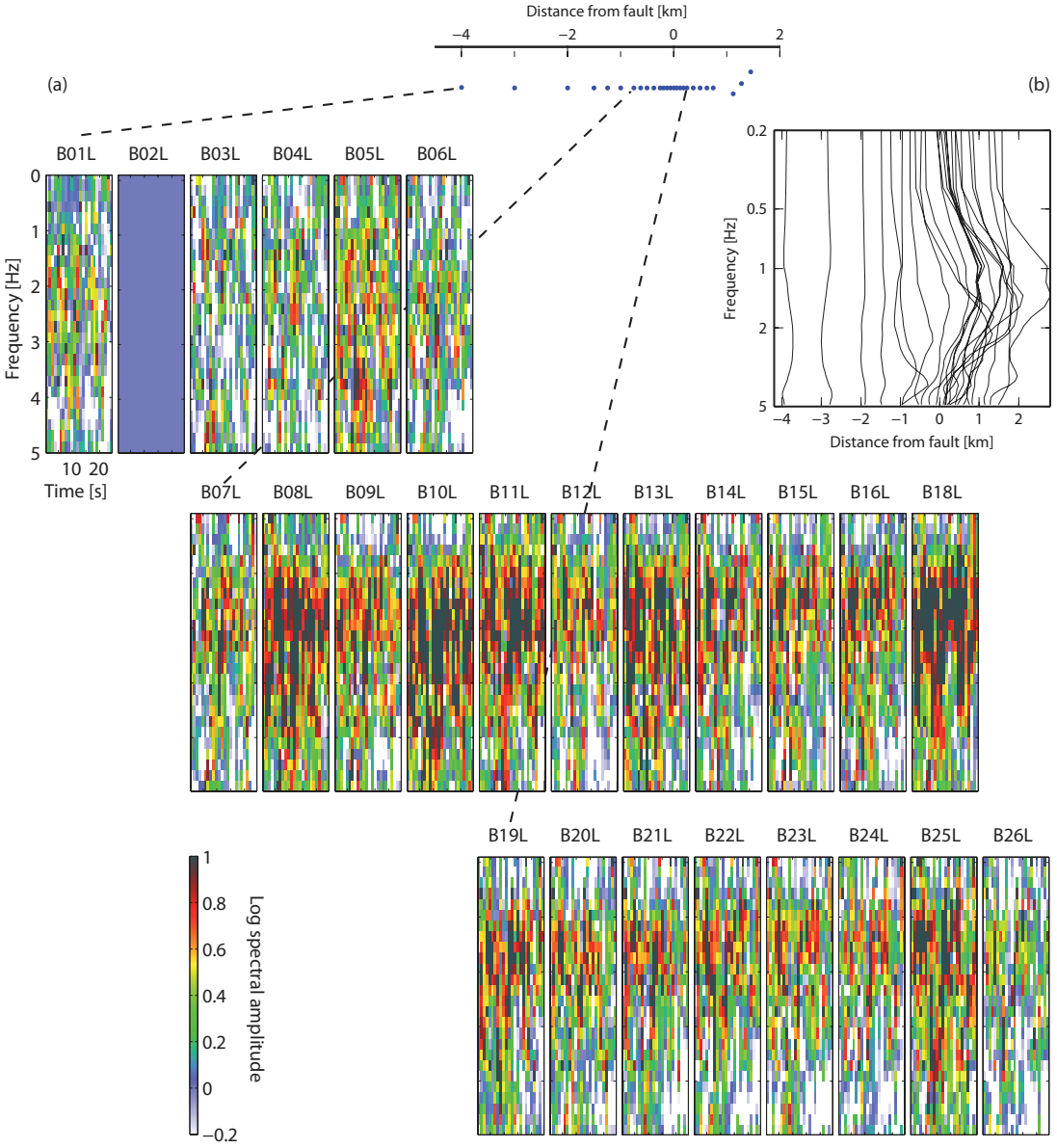

Figure S1: (a) Fault-normal distribution of vertical component spectral amplitudes associated with fault zone ballistic trapped waves. Spectrograms show relative amplitudes between 0–5 Hz in the 20 s after the P-wave arrival associated with a local earthquake [*Cochran et al.*, 2009]. Values in each pixel in each panel are scaled by B02L data located 3 km to the SW of the fault. (b) Average frequency dependent amplitude as a function of position. Each spectrum represents the average over the 20 s window in (a), averaged over five earthquakes/shots [*Cochran et al.*, 2009]. Spectra are scaled by an average spectrum associated with seismograms recorded at $x \leq 2$ km. Note that the scale of the ordinate is logarithmic, in contrast to the linear scale in (a), to enhance the visibility of the critical frequency for interaction, f_c. The high similarity of the spectra around $x = 0$ km to the scaled spectra constructed from noise correlations (main text Fig. 2) indicates a consistent frequency dependence for fault zone-wave field interaction for ballistic and scattered modes of propagation.

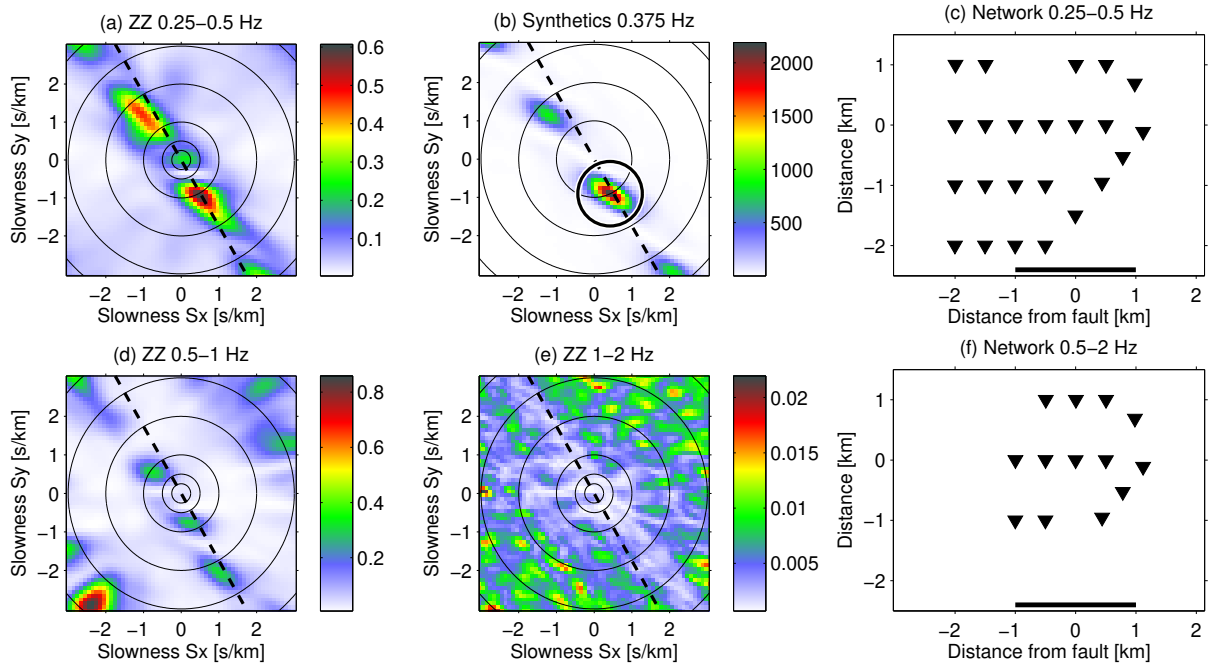

Figure S2: (a) Beamformer output for low-frequency ZZ correlations (same as main text Fig. 5a). The dashed line approximates the orientation of the Calico fault strike. Although coherent energy propagates in fault-normal directions, the algorithm is most sensitive to along-strike components [*Zhang and Gerstoft*, 2014]. Small modifications of the station distribution emphasize the near-vertical arrival in the center over the along-strike component. The array response (b) to synthetics with the same azimuth and slowness (encircled) indicates that secondary features in (a) do not correspond to propagation of energy. (c) We used the entire array with a homogenized spatial sampling. (d) Slow energy in fault-normal directions is found at intermediate frequencies, but beamforming is sensitive to processing choices and changes in the network configuration because of superimposed modes of propagation. (e) Propagation directions are randomized at high frequencies (same as main text Fig. 5b). (f) For $f > f_c$ an in-fault network is used. The black line in (c) and (f) indicates the approximate extension of the low velocity zone. Beamformer outputs are scaled by the length of the frequency vector and the number of stations. In (b) only one frequency is used. The dashed line indicates the orientation of the Calico fault strike.

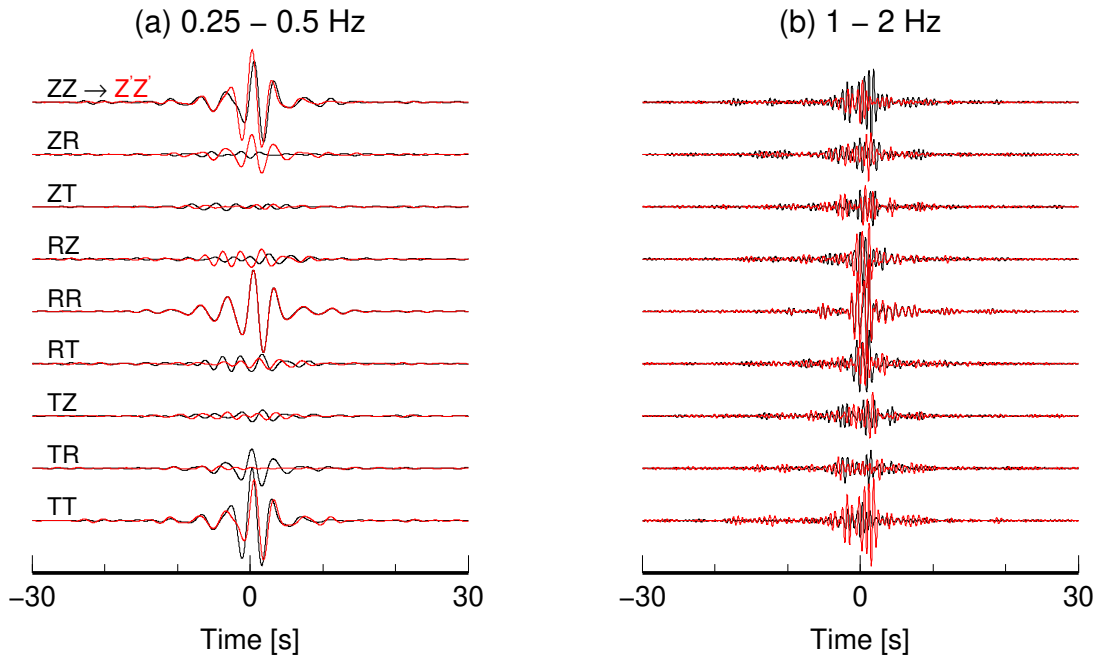

Figure S3: Effect of the Optimal Rotation Algorithm on the correlation tensor for low and high frequencies. Correlations correspond to two stations oriented in the fault-normal direction at -4 km and -0.5 km. Black and red traces indicate original and rotated correlations, respectively. Data are scaled to the maximum tensor amplitude. At low frequencies, station wise angles of $[11, 11]^{\circ}$ minimize energy on the TR component and enhance energy on the ZR component. At high frequencies, the rotation $[17, 23]^{\circ}$ cannot minimize energy on transversal components. This indicates that the wave field is not dominated by surface waves, but consists of a superposition of (scattered) surface and body waves.

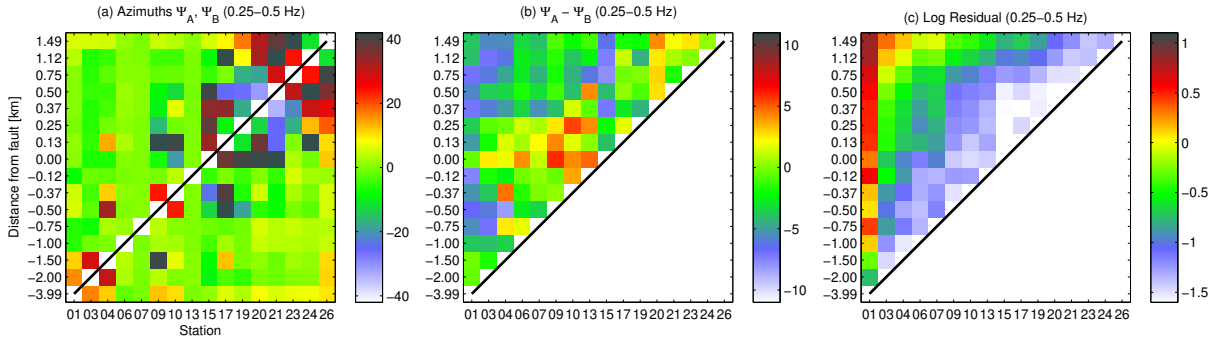

Figure S4: Collective representation of results from the Optimum Rotation Algorithm. Compare to Figure 5 in *Roux* [2009]. The left matrix (a) shows the pair wise distribution of rotation angles in the horizontal plane (azimuths Ψ). The abscissa contains the broadband station name (number 01–26). The ordinate indicates the associated distance from the fault trace. Angles for one pair are mirrored at the black line, e.g., azimuths for station pair 04/20, at a distance of -1.50/0.37 km are given at index $[3, 11]$ and $[11, 3]$. The long-range and short-range averages in main text Figures 4b, c are constructed from these data. The center matrix (b) shows the difference. The warm colors in the center around $x = 0$ indicate the effect of the fault. The right matrix (c) indicates the logarithm of the misfit, where small values indicate successful reduction of energy on ZT, RT, TZ, TR traces. Colorbars in (b) and (c) correspond to data in the upper left triangle.

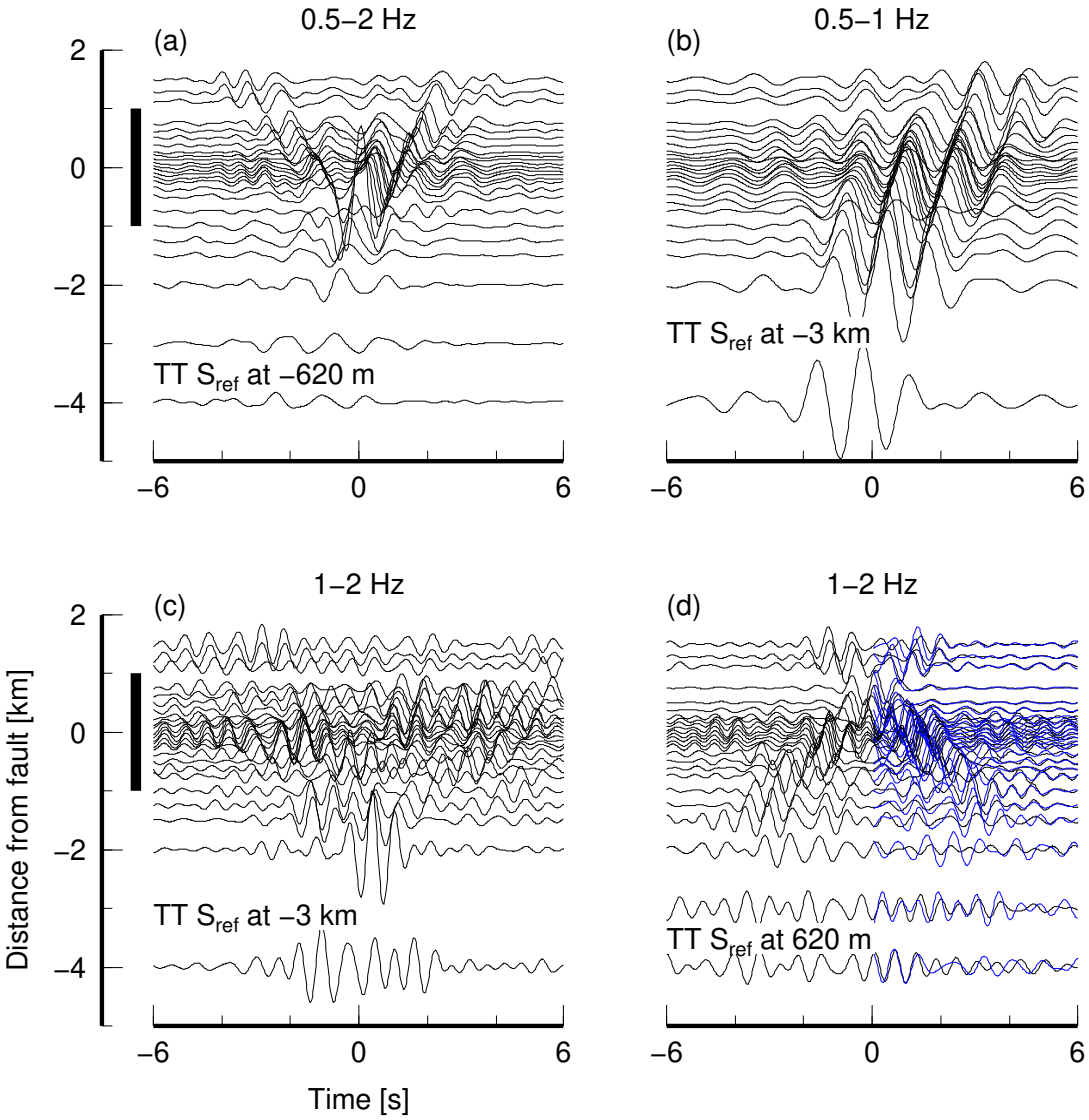

Figure S5: Frequency dependent correlation amplitude patterns are complementary to main text Figure 3. Amplitudes are scaled to the pattern maximum (a–c) or to the maximum of each trace (d). The ordinate corresponds to the abscissa in main text Figure 1b. Energy at negative (positive) times propagates towards (away from) the correlation reference station S_{ref}. (a) The broadband $f > f_c$ 0.5–2 Hz pattern contains a superposition of components typical for the intermediate (directional high-v_a arrival) and high frequency regime (symmetric in-fault amplitudes). (b) The wave field is coherent across fault zone boundaries at intermediate frequencies, (c) but not for high frequencies. (d) The X-shaped in-fault arrival pattern indicates trapped, isotropic noise. Note the increased symmetry for in-fault correlations indicated by the similarity between the black and blue waveforms, where the blue waveform is the average of negative and positive lag data. At distances smaller than -1 km, i.e., outside the low velocity zone, the similarity (amplitude and phase) is significantly reduced, which is an indicator for incoherent wave fields across the velocity gradient. Larger amplitudes at negative lag times and at -1 km is associated with energy arriving from West propagating towards S_{ref}.

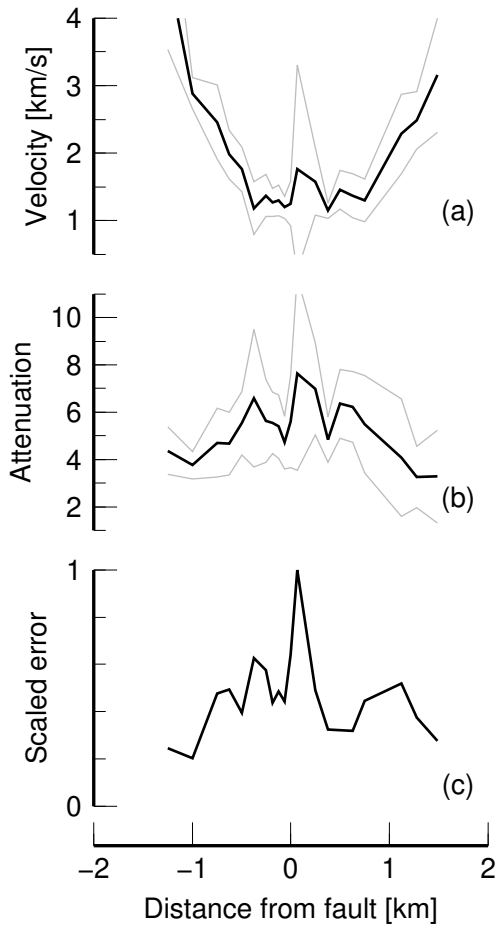

Figure S6: Results from fitting an attenuated Bessel function to 1–2 Hz ZZ focal spot amplitude distributions for positions in fault normal directions. (a) Fault-normal phase velocity estimates obtained from $k = \omega/c$, with $\omega = 2\pi 1.5$ 1/s. Reproduced from main text Figure 4e. (b) Associated estimates of the attenuation coefficient α. (c) RMS errors are scaled to the maximum value.

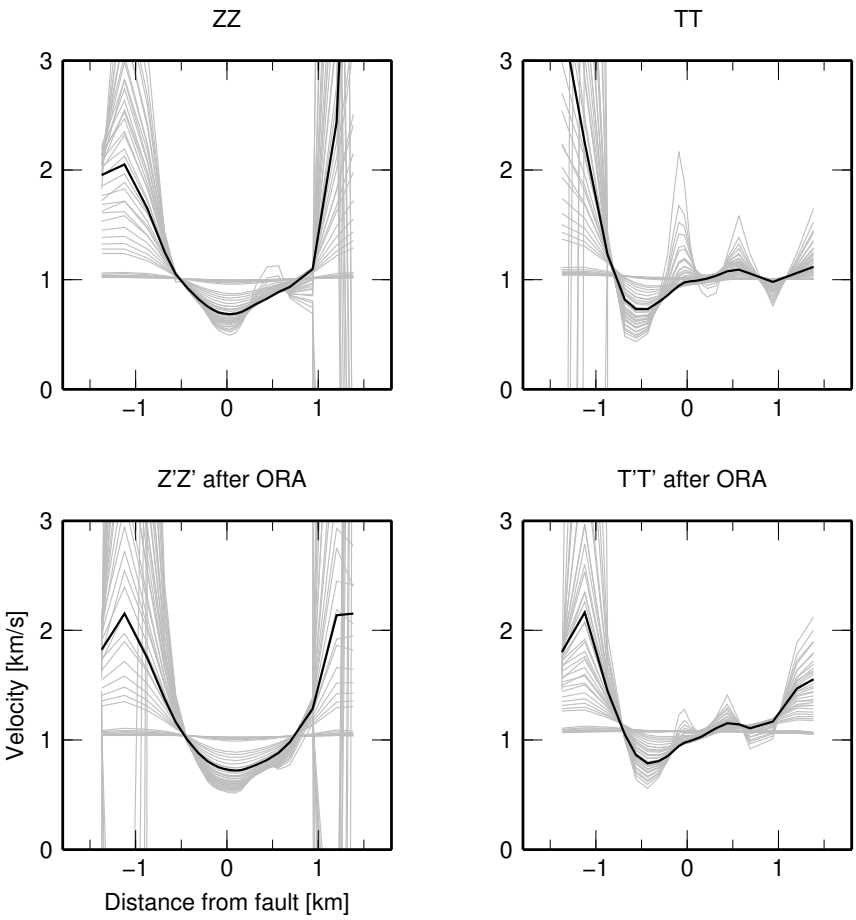

Figure S7: Individual (grey) and best (black) solutions of the 1–2 Hz phase velocity inversion. The search space includes a range of the tuning parameters λ and σ. Results in the top and bottom row are based on original correlations and correlations after the Optimal Rotation Algorithm applied. Rotation mostly affects estimates outside the LVZ at $|x| > 1$ km, which is due to wave field changes across the velocity gradient (ray bending).